

Accepted Manuscript

The speciation of thallium in (Tl,Sb,As)-rich pyrite

Luke L. George, Cristian Biagioni, Giovanni Orazio Lepore, Maria Lacalamita, Giovanna Agrosi, Gian Carlo Capitani, Elena Bonaccorsi, Francesco d'Acapito

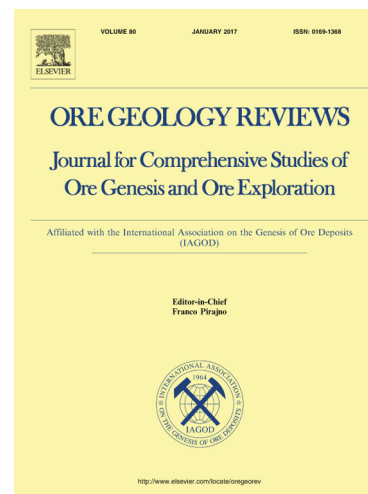
PII: S0169-1368(18)30935-1
DOI: <https://doi.org/10.1016/j.oregeorev.2019.02.031>
Reference: OREGEO 2846

To appear in: *Ore Geology Reviews*

Received Date: 7 November 2018
Revised Date: 18 February 2019
Accepted Date: 25 February 2019

Please cite this article as: L.L. George, C. Biagioni, G.O. Lepore, M. Lacalamita, G. Agrosi, G.C. Capitani, E. Bonaccorsi, F. d'Acapito, The speciation of thallium in (Tl,Sb,As)-rich pyrite, *Ore Geology Reviews* (2019), doi: <https://doi.org/10.1016/j.oregeorev.2019.02.031>

This is a PDF file of an unedited manuscript that has been accepted for publication. As a service to our customers we are providing this early version of the manuscript. The manuscript will undergo copyediting, typesetting, and review of the resulting proof before it is published in its final form. Please note that during the production process errors may be discovered which could affect the content, and all legal disclaimers that apply to the journal pertain.



The speciation of thallium in (Tl,Sb,As)-rich pyrite

Luke L. George^{a*}, Cristian Biagioni^{a†}, Giovanni Orazio Lepore^b, Maria Lacalamita^a,
Giovanna Agrosi^c, Gian Carlo Capitani^d, Elena Bonaccorsi^a, Francesco d'Acapito^b

^a Dipartimento di Scienze della Terra, Università di Pisa, Via S. Maria 53, I-56126 Pisa, Italy

^b CNR-IOM-OGG, 71 Avenue des Martyrs, F-38043 Grenoble, France

^c Dipartimento di Scienze della Terra e Geoambientali, Università degli Studi di Bari "Aldo Moro",
via Orabona 4, I-70125 Bari, Italy

^d Dipartimento di Scienze dell'Ambiente e di Scienze della Terra, Università degli Studi di Milano-
Bicocca, Piazza della Scienza 4, I-20126 Milano, Italy

Abstract

Three samples of (Tl,Sb,As)-rich pyrite from the ore deposits of southern Apuan Alps (Tuscany, Italy) were studied through a multi-technique approach in order to constrain the speciation and incorporation mechanism of thallium in pyrite. High concentrations of Tl, Sb, and As were detected in all the studied samples through laser ablation inductively-coupled plasma mass spectrometry (LA-ICP-MS). Average Tl contents were 1,299 ppm, 1,967 ppm, and 2,623 ppm in samples from Sennari, Canale della Radice, and Fornovolasco, respectively. The LA-ICP-MS time-resolved down-hole ablation profiles were smooth indicating that Tl, Sb, and As are dissolved in the pyrite matrix, or occur in homogeneously distributed nanoparticles (NPs). X-ray absorption spectroscopy (XAS) data revealed that Tl, Sb, and As occurs as Tl^+ , Sb^{3+} , As^{3+} , and As^{1-} . In all the studied samples, bond distances and coordination numbers for Sb^{3+} and As^{3+} are constant, whereas Tl displays a range of coordination numbers (~3 to ~6), revealing the occurrence of different local environments. Moreover,

* Luke George present address: School of Chemical Engineering, The University of Adelaide, Adelaide S.A. 5005, Australia

† Corresponding author: Cristian Biagioni cristian.biagioni@unipi.it

no hints of features corresponding to coordination shells higher than the first were observed, suggesting an extremely disordered environment around Tl. Transmission electron microscopy (TEM) investigations revealed the presence of dislocations and As-rich “fluid” inclusions, whereas no Tl-rich NPs were observed. The study suggests that Tl^+ could occur in structural defects in pyrite, lacking any long-range order. The ‘loose’ nature of Tl in pyrite favours its ready loss during the metamorphic recrystallization of pyrite and its redistribution within ore bodies and country rocks, with important implications from an economic and environmental point of view.

Key-words: pyrite; thallium; speciation; LA-ICP-MS; XAS; TEM

1 Introduction

Thallium has received much scientific attention over the last few decades, given that even low concentrations are highly toxic for humans, more toxic than As, Hg, Cd or Pb (e.g., Nriagu, 1998; Peter and Viraraghavan, 2005). Thallium tends to bioaccumulate in living organisms once it enters the biosphere (Karbowska, 2016), making it a dangerous contaminant in the environment. As such, Tl has been classified as one of the 13 priority metal pollutants (Keith and Telliard, 1979).

Although the crust is richer in Tl (average continental crust concentration of 0.52 ppm - Wedepohl, 1995) than, for example, Ag or Au, this element is rarely concentrated in significant abundance as other metals may be. Having both lithophile and chalcophile geochemical behaviour, Tl is generally dispersed within minerals. Given the similarity in ionic radii of Tl^+ and K^+ (1.70 Å and 1.64 Å in twelve-fold coordination, respectively - Shannon, 1976), Tl commonly substitutes for K in feldspars and phyllosilicates. Moreover, the ionic radius of Tl^+ is very close to that of NH_4^+ (e.g., Zelenski et al., 2009) and consequently it could occur in rocks enriched in organic matter, especially under reducing conditions.

Thallium may become significantly concentrated in sulphides, as proved by the large amounts of Tl occurring in some sulphide mineral deposits. For instance, Xiangquan, China, the world’s solitary Tl-only mine, hosts around 250 tons of Tl (Zhou et al., 2005), whereas Meggen, Germany,

contains 960 tons of Tl, the largest accumulation on Earth (Laznicka, 2010). Thallium is mainly produced as a by-product of pyrite-rich ore smelting (e.g., Peter and Viraraghavan, 2005) and, indeed, up to 3.5 wt. % Tl is hosted in some pyrite from Xiangquan, clearly demonstrating the ability of pyrite to host significant concentrations of this heavy metal.

Recently, the Tl-rich nature of several small pyrite \pm baryte \pm iron oxide ores hosted in the metamorphic units of the southern Apuan Alps (northern Tuscany, Italy) was recognised (e.g., Biagioni et al., 2013; D'Orazio et al., 2017). This is primarily expressed as Tl-rich pyrite (some pyrite samples concentrate over 4,200 ppm Tl - George et al., 2018a), and as assemblages comprising rare Tl-sulfosalts (e.g., Orlandi et al., 2012, 2013; Biagioni et al., 2014) mobilised in part as Tl-rich melts after release from pyrite during greenschist facies metamorphic recrystallization (Biagioni et al., 2013; George et al., 2018a). Release of Tl from pyrite due to oxidation has also caused severe Tl contamination in both stream waters and a public water supply system in the vicinity of the Apuan Alps pyrite ores (e.g., Biagioni et al., 2017; D'Orazio et al., 2017).

Despite pyrite being such an important Tl host worldwide, and its potential to release Tl into the environment under a range of physico-chemical conditions, the speciation of Tl in pyrite has never been unequivocally determined. Monovalent Tl should be the dominant oxidation state for Tl in most natural environments (Vink, 1993; Xiong, 2007). Nevertheless, trivalent Tl, the other naturally occurring oxidation state of Tl, may be stabilized by the anionic complexes Cl^- or OH^- (Batley and Florence, 1975), or oxidized from Tl^+ by Tl-oxidizing bacteria or UV irradiation (Karlsson et al., 2006). As such, some authors have suggested a trivalent, or even native occurrence, of Tl in pyrite (e.g., Huston et al., 1995; Zhou et al., 2005). Moreover, it has not been clearly shown whether Tl enters the crystal structure of pyrite or tends to occur as micro- to nano-particles of Tl-bearing phases. Deditius and Reich (2016) reported a wedge-shaped trend on a Tl vs. As plot, similar to the trend observed by Reich et al. (2005) for Au vs. As. This was interpreted to define a field where concentrations of Tl are likely present in solid solution, and thus that the solid solubility of Tl in pyrite is strongly dependent on As concentration. Similarly, George et al. (2018a) showed an approximately one-to-one correlation between (Tl + Cu + Ag) and Sb in pyrite from the southern Apuan Alps ore deposits, possibly indicating that Tl (as well as Cu and Ag) could be hosted in pyrite following the

substitution mechanism $2\text{Fe}^{2+} \leftrightarrow \text{Tl}^+ + \text{Sb}^{3+}$. However, as will be discussed below, the difference in ionic radius between Fe on the one hand, and Tl and Sb on the other, is likely too large and the proposed substitution mechanism seems difficult to envision.

Thus, Deditius and Reich (2016) suggested that further work was necessary to elucidate the speciation of Tl in pyrite. The aforementioned authors recommended that such efforts should combine determination of Tl composition and depth-profiling by laser ablation inductively-coupled plasma mass spectrometry (LA-ICP-MS), transmission electron microscopy (TEM) studies to detect the presence of any potential nano-particles, and synchrotron-based X-ray absorption near edge structure (XANES) and extended X-ray absorption fine structure (EXAFS) studies to determine the oxidation state and the local bonding environment of Tl.

Here, we attempt to combine these different methods (LA-ICP-MS, XANES, EXAFS, and TEM) in order to determine the speciation of Tl in the (Tl, Sb, As)-rich pyrite from the southern Apuan Alps. We report XANES and EXAFS data for Tl, as well as for Sb and As. Moreover, LA-ICP-MS and TEM investigations were made with the aim to determine if Tl is hosted in the pyrite crystal structure, or in micro- to nanoparticles (NPs) of other Tl-bearing phases. Understanding the speciation of Tl in pyrite is important since it should help clarify the mechanisms of release and dispersion of Tl in natural systems, particularly during pyrite oxidation, with significant environmental implications.

2 Sample material

Three Tl-rich pyrite samples, previously investigated by George et al. (2018a), were used in this study. One was collected from Sennari (SEN1), a small occurrence of pyrite cropping out on the road from Sant'Anna di Stazzema to Case Sennari, in the southern Apuan Alps, Tuscany, Italy. Another sample came from the Canale della Radice mine (sample CDR4) and the last from the Fornovolasco mine (sample FOR19). These two mines exploited small orebodies belonging to a series of pyrite \pm baryte \pm iron oxide ore deposits located within a \sim 10 km NE-SW belt in the southern Apuan Alps (D'Orazio et al., 2017 and references therein). The Apuan Alps represent a tectonic

window exposing the most complete succession of northern Apennine units in a complex tectonic nappe formed due to numerous over-thrusts during the Tertiary Apennine Orogeny (Fellin et al., 2007 and references therein).

The orebodies at Canale della Radice and Fornovolasco were mostly monomineralic lens-shaped bodies with pyrite or magnetite and minor baryte. The geological setting of these deposits is described in D'Orazio et al. (2017) and references therein. The orebodies were metamorphosed to the greenschist facies during the Apennine Orogeny, partly remobilising the ore and recrystallizing pyrite (George et al., 2018a and references therein). While the Sennari sample does not come from a mine, it is hosted in the same metamorphic units and shares similar mineralogy, textures and pyrite geochemistry to samples from Apuan Alps deposits (George et al., 2018a).

SEN1 contains networks and bands of very fine to fine subhedral to anhedral pyrite in baryte, benstonite and lesser ankerite (Fig. 1A); accessory cymrite was observed. Pyrite sometimes forms granoblastic aggregates (Fig. 1B). CDR4 hosts coarse, sometimes granoblastic, aggregates and disseminations of very fine to fine grained euhedral to anhedral pyrite (Fig. 1C, D), sometimes aligned in rough bands. Some medium to coarse-grained relict euhedral pyrite and very fine grained framboidal pyrite is also present. Matrix minerals include siderite, dolomite, “chlorite”, “biotite”, cymrite, albite and quartz. FOR19 contains very coarse grained colloform banded pyrite (Fig. 1E, F) and lesser fine grained anhedral pyrite in siderite, dolomite and quartz. In some places, finer grained pyrite is being replaced by pyrrhotite and arsenopyrite.

3 Methodology

3.1 Laser ablation inductively-coupled plasma mass spectrometry (LA-ICP-MS)

LA-ICP-MS data were collected using an ASI M-50-LR 193 nm Excimer laser attached to an Agilent 7700cx Quadrupole inductively coupled-mass spectrometer (Adelaide Microscopy, University of Adelaide) following the methods set out in George et al. (2018a). LA-ICP-MS spot analyses were used for accurate quantitative concentration measurements and monitoring of potential micro- to

nano-inclusions in pyrite using time-resolved down-hole ablation profiles. LA-ICP-MS element mapping was used to monitor trace element variation and zonation. Laser repetition rate was maintained at 5 Hz for spot analysis and 10 Hz for mapping. The total acquisition time for each individual spot analysis was 70 s: 30 s of background measurement followed by 40 s of sample ablation. For mapping, a 10 s background measurement was acquired before the ablation of each trench. A 20 s delay time was allowed after each spot or trench analysis to ensure the ablation cell was sufficiently washed-out and the gases had stabilized.

During spot analysis and mapping, the following suite of isotopes were measured: ^{27}Al , ^{29}Si , ^{43}Ca , ^{49}Ti , ^{53}Cr , ^{55}Mn , ^{57}Fe , ^{59}Co , ^{60}Ni , ^{65}Cu , ^{66}Zn , ^{69}Ga , ^{71}Ga , ^{75}As , ^{77}Se , ^{95}Mo , ^{107}Ag , ^{111}Cd , ^{115}In , ^{118}Sn , ^{121}Sb , ^{125}Te , ^{137}Ba , ^{182}W , ^{197}Au , ^{202}Hg , ^{205}Tl , ^{206}Pb , ^{207}Pb , ^{208}Pb and ^{209}Bi . During spot analysis, the dwell time for most elements was set at 0.02 s, while Se, Au and Tl were set at 0.04 s, Co, Ni, Cu and Zn were set at 0.01 s and Al, Si, Ca, Mn, Fe and Ba were set at 0.005 s. Aluminium, Si, Ca and Ba counts were monitored to ensure gangue phases were not analysed; these elements were not quantified. During mapping, the dwell time for most elements was 0.01 s, while Ti, Cr, Mn, Co, Ni, Cu, Zn, As, Ba, Pb and Bi were set at 0.005 s and Al, Si, Ca and Fe were set at 0.002 s.

Two 51- μm analyses were made on the STDGL3 standard (Belousov et al., 2015) every 20 unknown spot analyses, as well as before and after a map acquisition. All data calculations were carried out using Iolite (Paton et al., 2011), an open source software package for ICP-MS data processing developed by the Melbourne Isotope Group as an add-in for the data analysis program Igor by WaveMetrics. Iron was used as the internal standard assuming stoichiometric pyrite.

3.2 X-ray absorption spectroscopy (XAS)

X-ray absorption spectroscopy (XAS) measurements on pyrite at the Tl L_3 -edge (12,658 eV), As K -edge (11,867 eV) and Sb K -edge (30,491 eV) were made at the LISA beamline (BM-08; d'Acapito et al., 2019) at the European Synchrotron Radiation Facility (ESRF, Grenoble, France) during three different experimental sessions. Pyrite was selected in order to avoid the gangue minerals and an aliquot of the powdered samples was checked through X-ray powder diffraction using a Bruker

D2 Phaser diffractometer operating at 30 kV and 10 mA (Ni-filtered Cu $K\alpha$ radiation) and equipped with a one-dimensional Linxeye detector. Pyrite was the only mineral above detection limit (> 1 vol%). However, the occurrence of minor amounts of accessory sulphides and gangue minerals cannot be avoided.

Since measurements were taken in a wide energy range, Pd- or Pt-coated mirrors were used for harmonics rejection ($E_{\text{cutoff}} \approx 18$ KeV and 40 KeV, respectively). Model compounds and sample material were powdered, mixed with cellulose and pressed in pellets. The amount of material used was such as to keep the maximum total absorption (μ) around 1.5. All samples were measured in fluorescence mode by means of a 12-element solid state (high purity Germanium) detector while all reference compounds, with the exception of protochabournéite at the Tl L_3 -edge (see text below), were measured in transmission mode. All the fluorescence detected data were deadtime corrected; in order to check for the presence of over-absorption effects, self-absorption corrections were run on collected spectra at all absorption edges in ATHENA (Ravel and Newville, 2005), using the FLUO (available on Daniel Haskel webpage at APS, <https://www3.aps.anl.gov/haskel/>) and Booth (Booth and Bridges; 2005) algorithms for XANES and EXAFS regions, respectively. Results of self-absorption corrections (see Appendix A) rule out the possibility of over-absorption effects since experimental and absorption-corrected data are essentially superimposed at all measured edges. In order to reduce the damping of the signal due to the thermal contribution and to prevent possible beam-induced redox reactions, all samples were measured at 80 K using a liquid N_2 cold finger cryostat (Puri et al., 2019).

Spectra at the Tl L_3 -edge were acquired in the energy range 12,458-13,206 eV. The energy sampling interval in the higher resolution near edge region (12,638–12,688 eV) was 0.5 eV. A fixed exit sagittally focusing monochromator (d'Acapito et al., 2014) with a pair of Si [311] crystals were used; beam size was ~ 2000 (H) $\mu\text{m} \times 150$ (V) μm . Measured reference compounds were Tl_2O_3 , protochabournéite ($\sim \text{Tl}_2\text{Pb}(\text{Sb}_{9-8}\text{As}_{1-2})_{\Sigma 10}\text{S}_{17}$ - Orlandi et al., 2013) and Tl_2SO_4 . Synthetic Tl_2O_3 and Tl_2SO_4 were collected in transmission mode. Suitable filters were used for fluorescence measurements in order to attenuate for Fe and As fluorescence emission. Pyrite samples bearing significant As, as well as protochabournéite, showed strong As fluorescence emission ($K\alpha_1 = 10,543$ eV) which almost

superimposes on the Tl emission line ($L\alpha_1 = 10,269 \text{ eV}$) considering that the energy resolution of the detector is about 300 eV . Therefore, spectra were collected with a Ga filter ($K\text{-edge} = 10,367 \text{ eV}$) associated with a $40 \mu\text{m}$ Al filter to damp the Ga fluorescence. The Ga filter was specifically prepared for this experiment by depositing Ga_2O_3 on various layers of teflon filters to obtain a thickness equivalent to $80 \mu\text{m}$ of Ga_2O_3 , absorbing most part of the fluorescence emission above the Ga $K\text{-edge}$. The teflon layers are very fragile and, probably due to the presence of holes and fractures in the filter, the final effect was closer to a filter with an equivalent thickness of $30 \mu\text{m}$ of Ga_2O_3 . The actual effect of the filter on transmissivity at the different energies is summarized in Appendix B; the count rate on the detector in the Tl emission region was $\sim 500 \text{ cts/s}$ (with total counts on the detector always lower than $10/20\text{k cts/s}$). The small Se amounts (Table 1) present in the samples were found to be below detection limit; besides, the Se emission line ($K\alpha_1 = 11,224 \text{ eV}$) is well separated from that of Tl and its emission would be mainly absorbed by the Ga filter. A Se (Se $K\text{-edge} = 12,657.8 \text{ eV}$) model compound was placed in a second experimental chamber, allowing simultaneous spectrum acquisition with each measurement on the samples and thus accurate energy calibration. A minimum of ten spectra were collected for each sample and no hints of beam damage effects were shown in each series of measurements.

For As investigation, samples were measured after the first part of the BM08 refurbishment (d'Acapito et al., 2019) using a pair of flat Si [111] monochromator crystals. Beam size was $\sim 2000 \text{ (H)} \mu\text{m} \times 150 \text{ (V)} \mu\text{m}$. Spectra were acquired in the energy range $11,667\text{--}12,850 \text{ eV}$. Seven As compounds were also measured as standards in transmission mode: skutterudite (CoAs_3), protochabournéite (As^{3+} sulphide), arsenopyrite (FeAsS), adamite ($\text{Zn}_2\text{AsO}_4\text{OH}$), orpiment (As_2S_3), As_2O_3 and As_2O_5 (hydrated).

For Sb investigation, samples were measured with the BM08 setup (d'Acapito et al., 2019), using a pair of flat Si [311] monochromator crystals and Pt coated focusing mirrors ($E_{\text{cutoff}} \approx 40 \text{ KeV}$). Beam size was $\sim 200 \text{ (H)} \mu\text{m} \times 200 \text{ (V)} \mu\text{m}$. Measured reference compounds were Sb_2S_3 , Sb_2O_3 and Sb_2O_5 . A reference Sb foil was also measured at the same time in order to accurately calibrate the energy. For each sample, six spectra were collected and no hints of beam damage effects were shown in each series of measurements.

The software ATHENA (Ravel and Newville, 2005) was used to average multiple spectra. Standard procedures (Lee et al., 1981) were followed to extract the structural EXAFS signal ($k\chi(k)$): pre-edge background removal, spline modelling of bare atomic background, edge step normalization using a far above the edge region, and energy calibration. Model atomic clusters centred on the absorber atom were obtained by ATOMS (Ravel, 2001); theoretical amplitude and phase functions were generated using the FEFF8 code (Ankudinov et al., 1998). EXAFS spectra were fitted through the ARTEMIS software (Ravel and Newville, 2005) in the Fourier-Transform (FT) space.

3.3 Transmission electron microscopy (TEM)

Transmission electron microscopy investigations were performed on the samples FOR19 and CDR4 (the samples having the highest average Tl content) at the Dipartimento di Scienze della Terra e Geoambientali of the University of Bari, and at the Dipartimento di Scienze Fisiche, della Terra e dell'Ambiente of the University of Siena, with two analogous JEOL-JEM 2010, having the following characteristics: operating voltage 200 kV, LaB₆ source, nominal point resolution of ~2.0 Å and spherical aberration of 0.5 mm. In order to distinguish between artefacts induced by sample preparation and the intrinsic micro/nano structures of the samples, two different methods, ion milling and grinding, were used. For ion milled mounts, the samples were prepared as 30 µm thick double polished petrographic thin sections using a hot melt adhesive to fix the mineral to the glass slide. Copper-rings, 3 mm in diameter, were then glued on selected areas of the sections using Araldite®. Once hardened, the rings and the underneath mineral were detached with the aid of a scalpel and a hot plate. The mineral was finally ion milled down to electron transparency with Ar ions in a Gatan Precise Ion Polishing System (PIPS) at the Dipartimento di Scienze della Terra of the University of Milan. Before TEM experiments, ion milled mounts were carbon coated to avoid electrostatic charging during observations. Some fragments from the same FOR19 sample were also manually ground in a carborundum mortar. The obtained powder was ultrasonically dispersed in acetone, thereafter a few drops of the suspension were deposited onto a 3 mm wide holey carbon Cu-grid. Both single and double-tilt specimen holders ($\pm 20^\circ$) were used for powdered samples and polished samples.

Digital images were recorded with a Gatan US 1000 CCD (Bari) and an Orius CCD camera (Siena). Energy-dispersive qualitative X-ray analyses (EDS) were obtained with Oxford Link (Siena) and Oxford-INCA (Bari) EDS spectrometers, both equipped with a Si(Li) detector and ultra-thin window. Quantitative analyses were obtained using the standard-less method within the Van Cappellen and Doukhan (1994) approximation.

High Resolution Transmission Electron Microscopy (HRTEM) images were rotationally filtered (Kilaas, 1998) with the HRTEM filter (Mitchell, 2007), as implemented in the Gatan Digital Micrograph version 3.9, in order to remove noise contrast from amorphous materials.

4. Results

4.1 Laser ablation-inductively coupled plasma-mass spectrometry (LA-ICP-MS)

Pyrite in all three samples contained high concentrations of Tl, Sb and As (Figure 2 and Table 1). On average, pyrite in SEN1 contained 1,299 ppm Tl, 1,299 ppm Sb and 364 ppm As, CDR4 pyrite hosted 1,967 ppm Tl, 1,871 ppm Sb and 1,857 ppm As, while FOR19 hosted 2,623 ppm Tl, 1,896 ppm Sb and 1,602 ppm As. Based on LA-ICP-MS mapping of a handful of samples from Canale della Radice and Fornovolasco, minor zoning of trace elements was only noted in some coarse inclusion-free late metamorphic pyrite, and the colloform bands in FOR19 (Figure 2B).

For elements hosted in solid solution in a mineral, LA-ICP-MS time-resolved down-hole ablation profiles will appear smooth, whereas sub-surface inclusions usually show as peaks on such profiles if they are sufficiently large and not homogeneously distributed (e.g., Cook et al., 2009; George et al., 2015, 2018b). Using Iolite, the LA-ICP-MS down-hole ablation profile for each element in each analysis was carefully checked for peaks that may indicate an inclusion was accidentally ablated. Overall, spectra were smooth. While some spectra revealed occasional tiny peaks that may be due to nano-inclusions of distinct phases, the selected time interval for integration always excluded tiny peaks (Figure 2). Thus, the LA-ICP-MS data may be assumed to reflect trace elements in solid solution or related to homogeneously distributed NPs. Especially for Tl, Sb and As, most LA-ICP-MS

down-hole ablation profiles appeared smooth, even those corresponding to exceptionally rich concentrations of Tl, i.e., colloform banded pyrite in FOR19 (Figure 2B and C). Similarly, LA-ICP-MS element maps revealed smooth distributions of Tl, Sb and As, even when some zonation is present, i.e., Figure 2B.

Figure 3A shows a positive correlation between Tl and Sb (as mol. %). Such a correlation may be explained by a coupled substitution between these elements into the pyrite structure, i.e., $2\text{Fe}^{2+} \leftrightarrow \text{Tl}^+ + \text{Sb}^{3+}$. George et al. (2018a) noted that Tl does not correlate well with As in pyrite from the southern Apuan Alps ore deposits, as shown here in Figure 3B. Pyrite in FOR19 and CDR4 typically contains far more As than Tl (comparing mol. %), likely reflecting the possible incorporation of anionic As as well as As^{3+} , in agreement with XANES data. Indeed, As^{-1} is the most common oxidation state of As in pyrite in deposits that are not oxidised, e.g., high-sulfidation epithermal and porphyry deposits (Simon et al., 1999a, 1999b; Savage et al., 2000; Reich et al., 2005, 2013; Deditius et al., 2008; Qian et al., 2013).

4.2 X-ray absorption spectroscopy (XAS)

4.2.1 Tl L_3 -edge

XANES spectra of measured samples and reference compounds indicate that Tl in pyrite is present as Tl^+ (Figure 4). Pyrite samples and protochabournéite show a single absorption peak, typical of monovalent Tl compounds (e.g., Scheckel et al., 2004; Agarwal and Vishnoi, 2005; Dutrizac et al., 2005; Peacock and Moon, 2012; Biagioni et al., 2017) at 12,663 eV (first derivative maximum) while Tl_2O_3 shows a weak peak, followed by a shoulder on rising absorption, culminating in a marked peak at 12,669 eV (first derivative maximum)..

Results of EXAFS quantitative analysis are shown in Table 2. Thallium L_3 -edge EXAFS and Fourier transforms of measured samples are shown in Figure 5; the corresponding multiparameter fits are also shown. Fit results (Table 2) indicate that Tl in the analysed pyrite samples has a first

coordination shell constituted by S atoms; attempts to fit the first shell with oxygen atoms or with a combination of S and O were unsuccessful. First shell distances show substantial variations among the three studied samples. Specifically, Tl–S distances are much lower in FOR19 pyrite compared to CDR4 and SEN1 pyrite. Given the high error on refined distances and the frequent extreme inhomogeneity of the Tl⁺ coordination environment (e.g., Sabrowsky et al., 1979; Gostojić et al., 1982; Orlandi et al., 2013), it is difficult to determine a precise coordination number (CN) for the studied samples. Nevertheless, a crystal chemical comparison of Tl–S distances in the studied samples with data on Tl minerals allows these results to be strengthened. Indeed, coordination numbers appear in agreement with those expected by the bond valence model (BVM; Brown and Altermatt, 1985), according to which the distance fitted in the quantitative analyses would be compatible with a coordination of ~3.2(2), 5.3(7) and 6.0(4) for FOR19, SEN1 and CDR4, respectively. The choice of the R_0 value (2.545 Å) proposed by Brown and Altermatt (1985) seems the most suitable for Tl–S bonds; Biagioni et al. (2014) have indeed noticed that the R_0 reported by Brese and O’Keeffe (1991), i.e. 2.63 Å, usually results in an overbonding of Tl and suggested an R_0 of 2.55 Å, almost identical to the one proposed by Brown and Altermatt (1985). Figure 6 shows the relationship between CN and Tl–S average bond distances taken from the Tl sites of several Tl minerals. The position of the studied samples fit well with data from the literature, confirming a substantially different environment for Tl between FOR19, which shows features similar to carlinite (Tl₂S - Giester et al., 2002), where Tl is at the vertex of a pyramid coordinating 3 S atoms, and CDR4 and SEN1, which appear more similar to phases such as raguinite (TlFeS₂ - Welz et al., 1989), ellisite (Tl₃AsS₃ - Gostojić, 1980) and fangite (Tl₃AsS₄ - Wilson et al., 1993) (Tl2 site), where Tl is hosted in 5/6-coordinated sites. Coordination numbers obtained by the EXAFS multiparameter fits and BVM are in excellent agreement with only a very small discrepancy shown by sample FOR19, thus supporting the choice of the bond valence parameters and the fact that no self-absorption effects played a significant role in the data collection.

No hints of features corresponding to coordination shells higher than the first could be distinguished in the EXAFS signal. This may be due to the quality of available data that could be related to an extremely disordered environment around Tl atoms or to the very small size of Tl-rich clusters within pyrite.

4.2.2 As K-edge

Measurements at the As K-edge were focused on the XANES region. Despite the fact that measurements were taken in vacuum at 80 K, there was no way to avoid the partial oxidation of As to As⁵⁺. The effect is clear by looking at the linear combination fit (LCF) results (Table 3) performed with ATHENA (Ravel and Newville, 2005), and it is evidenced by the presence of a small bump on the measured spectra at ~11874 eV, in correspondence of the main edge crest of adamite [Zn₂(AsO₄)(OH)] (Figure 7). All the studied samples' spectra can indeed be approximated by a combination of arsenopyrite, protochabournéite, and adamite (see Table 3 and Figure 7). The oxidation was markedly evident for FOR19 where oxidation gradually increased after each measurement, while in the case of SEN1 and CDR4 the process does not seem to increase with the exposure time. This effect is illustrated in Appendix C, where the gradual oxidation of As in sample FOR19 in three consecutive measurements is shown. Data indicated that As oxidises mainly at the expense of arsenopyrite, while the contribution of As³⁺ sulphide does not seem to change with the exposure to the beam. According to the correlation observed in Appendix A, the oxidized contribution should reach the 0 value with an arsenopyrite content of ~0.8 (relative fraction of total As), which would be in good agreement with the approximately constant value of As³⁺ sulphide of ~0.2. As a consequence of this effect, only the first measured spectrum has been used for the analysis of sample FOR19, while the sum of four consecutive spectra was employed for the other samples.

It is reasonable to conclude that all the “arsenate” contributions in pyrite highlighted by the LCF is likely due to the oxidation of As during the preparation of the pellets and exposure to the X-ray beam. Indeed, following the mineralogical characterization performed by George et al. (2018) on these samples, the occurrence of natural arsenates seems to be unlikely. The contribution of the As⁵⁺ component is not always negligible, nonetheless it is possible to infer that As is present at least as both As⁻¹ and As³⁺, the latter bonded to S.

4.2.3 Sb K-edge

XANES spectra at the Sb *K*-edge for measured samples and standards are shown in Figure 8. The edge position clearly indicates that Sb is present in the trivalent state with all the studied samples having the maximum of the first derivative at 30,492.1 eV, in perfect agreement with that shown by Sb₂S₃. Sb *K*-edge EXAFS and Fourier transform of measured samples and standard compounds are shown in Figure 9, as are the corresponding multiparameter fits; fit results are shown in Table 4. Both the period of oscillations and the position of the main peak in the Fourier transform space indicate considerable similarity between the studied samples and pure Sb₂S₃. The EXAFS quantitative analyses (see Table 4) shows that Sb has a first coordination shell constituted by S atoms; first shell distances show no substantial variations among the three studied samples and are very similar to those of Sb₂S₃. On the contrary, it is possible to notice from Figure 9 how the spectrum of Sb₂O₃ shows a markedly different oscillation period. Nonetheless, attempts to fit the first shell with oxygen atoms or with a combination of S and O were tentatively tried resulting unsuccessful.

4.3 Transmission electron microscopy (TEM)

The TEM-EDS investigations on samples CDR4 and FOR19 revealed different nano-structural features. The prominent ones are dislocations which appear either long and curved, straight and long, or short and straight (Figure 10A). The different appearance of the dislocations may be due to different operating Burgers vectors and to different orientations of the dislocation lines (Figure 10A, B). High resolution images of short and straight dislocations, tagged with black arrows in Figure 10A, were taken along $[0\bar{1}1]$ and showed (011) lattice planes offset by $\frac{1}{2} [011]$ from one side to the other of the dislocation line (Figure 10C, D).

Another nano-structural feature of the investigated samples is the occurrence of “fluid” inclusions with polygonal shape (Figure 11). High-resolution images of the inclusions taken along $[0\bar{1}1]$ show they are confined within the {011}, {111}, and {100} crystallographic planes of pyrite (Figure 11). The absence of lattice fringes other than those of pyrite and/or moiré suggests that no

crystalline precipitate is present within the inclusions. The attenuation, up to disappearance, of lattice fringes towards the interior of the inclusions indicates that these inclusions may contain amorphous material. Qualitative EDS chemical data indicate an As-rich nature of these inclusions (Figure 12A).

TEM-EDS analyses reveal no significant compositional differences between defect-free pyrite and pyrite showing dislocations. Arsenic is homogeneously distributed, even if areas with high density of “fluid” inclusions show a significant As-enrichment, up to 2.4(5) wt% (Figure 12A). Thallium content is generally below the detection limit for TEM-EDS. However, some areas of the ground sample FOR19 exhibit locally detectable levels of Tl [1.9(8) wt%] and Sb [0.8(2) wt%] (Figure 12B). Unfortunately, these areas are too thick to obtain images with microstructural contrasts.

5. Discussion

5.1 A step in the understanding of thallium speciation in pyrite

In accord with previous investigations (e.g., D’Orazio et al., 2017; George et al., 2018a), Table 1 shows the complex geochemistry of pyrite samples from the southern Apuan Alps ore deposits, having variable amounts of trace elements. These trace elements may be incorporated into pyrite through complex mechanisms and their speciation and concentration are controlled by several factors (e.g., Reich et al., 2005; Deditius et al., 2014; Deditius and Reich, 2016). In particular, two types of speciation can be identified, i.e. structurally bound elements vs. nanoparticle-hosted elements. Several crystal-chemical considerations (i.e., atomic radii, formal charges) constrain the possibility of hosting elements in the crystal structure of pyrite, whereas NPs can have varying degrees of crystallinity (e.g., amorphous Fe-As-S inclusions in arsenian pyrite from Pueblo Viejo, Dominican Republic – Deditius et al., 2009) and complexity, i.e., from native elements to complex nanophases (e.g., Deditius et al., 2011).

5.1.1 Thallium in pyrite from the southern Apuan Alps ore deposits and the role of As and Sb

The high Tl content of pyrite ores from the ore deposits of the southern Apuan Alps was first noted by Biagioni et al. (2013) and fully described by D'Orazio et al. (2017). George et al. (2018a) detailed the geochemical evolution of pyrite during metamorphic recrystallization and the relationships occurring among several hosted elements, suggesting the potential role played by the coupled heterovalent substitution $2\text{Fe}^{2+} \leftrightarrow \text{Tl}^+ + \text{Sb}^{3+}$. Indeed, SEM observations of pyrite samples and the smooth nature of the LA-ICP-MS profiles did not reveal the occurrence of Tl-bearing inclusions. These results agree with previous studies on Tl-bearing pyrite, that were not able to detect the occurrence of Tl-bearing NPs (e.g., Kouzmanov et al., 2010), suggesting that Tl preferentially dissolves in the pyrite matrix. However, as noted by Cook et al. (2009), the occurrence of homogeneously distributed NPs of Tl-bearing phases (only few tens of nanometers in size) could lead to misinterpretation of the LA-ICP-MS data.

Previous authors suggested that the occurrence of anionic or cationic As species (As^{-1} , Simon et al., 1999a; Abraitis et al., 2004; As^{3+} , Deditius et al., 2008), as well as cationic Sb (Sb^{3+} , George et al., 2018a), favours the incorporation of several trace elements in pyrite as a result of the combination of electrical (*p*-type conductivity vs *n*-type conductivity) and crystal-chemical (expansion of the unit cell and creation of structural distortion) effects that As and Sb may induce in pyrite. In addition, another important factor controlling the concentration of trace elements in pyrite is the crystal size: the smaller the crystal size the larger is the specific surface is, which favours the adsorption of trace elements. However, nanoparticulate semiconductors experience self-purification, expelling non-stoichiometric impurities toward grain boundaries (Erwin et al., 2005 and references therein). Consequently, for trace elements incorporation from adsorption, the growth rate of pyrite must exceed the equilibration and removal rate of trace elements. The fine crystal size and the colloform banded texture shown by pyrite from the ore deposits of southern Apuan Alps suggest it formed through pristine kinetically-controlled crystallization under lower *T* conditions, promoting the distortion of the pyrite structure and the incorporation of abundant trace elements. This incorporation is likely further favoured by the occurrence of Sb^{3+} , as first proposed by George et al. (2018a).

5.1.2 Speciation of thallium in pyrite

Whereas some authors proposed the occurrence of Tl^{3+} in collomorphic pyrite (Huston et al., 1995), EXAFS and XANES data proves that Tl is present as Tl^+ . This valence state is the most common in natural Tl compounds; indeed, among the 69 known Tl minerals, only three contain Tl^{3+} , i.e. avicennite, Tl_2O_3 , chrysothallite, $\text{K}_6\text{Cu}_6\text{Tl}^{3+}\text{Cl}_{17}(\text{OH})_4\cdot\text{H}_2\text{O}$, and kalithallite, $\text{K}_3\text{Tl}^{3+}\text{Cl}_6\cdot 2\text{H}_2\text{O}$. The occurrence of Tl^+ in pyrite from southern Apuan Alps ores is coupled with the presence of Sb^{3+} and As^{3+} , as indicated by XAS data. Arsenic also occurs as As^{-1} , implying a dual crystal-chemical role for this element in the studied samples. The role played by trivalent Sb and As in favouring the incorporation of Tl^+ in pyrite agrees with previous data reported by Deditius and Reich (2016).

EXAFS data indicate that the thallium coordination numbers range from ~ 3 to ~ 6 in the studied samples, thus differing from the usually higher coordination numbers observed in sulfosalts (e.g., Makovicky, 2018). Thus the occurrence of sulfosalt NPs may be excluded.

The Tl–S distances are in the range $\sim 3\text{--}3.2$ Å, significantly larger than Fe–S distances (~ 2.26 Å, Rieder et al., 2007). Arsenic–S and Sb–S distances are ideally 2.26 and 2.45 Å. In agreement with XAS data, these two elements display the typical trigonal pyramidal coordination, observed in As^{3+} and Sb^{3+} -compounds. The range of different Tl coordination numbers among the three studied samples indicate the occurrence of different local environments around this element. This observation is not compatible with a simple coupled substitution $2\text{Fe}^{2+} \leftrightarrow \text{Tl}^+ + \text{Sb}^{3+}$. Indeed, assuming the incorporation of Tl through this substitution, the same local environment around Tl should be observed in all the studied samples. Moreover, the complete lack of signal about coordination shells higher than the first in the EXAFS signal may be hypothetically related the occurrence of an extremely disordered environment around Tl atoms, possibly with the absence of long-range order, i.e., an amorphous environment. This is not entirely surprising, since the replacement of Fe by Tl would cause too short metal–S distances, requiring an important reorganization of the local structure of pyrite. TEM imaging revealed a number of defects affecting the pyrite structure, such as dislocations and “fluid” inclusions, but no Tl enrichment could be detected on these defects, since Tl was always below the detection limit as in defect-free pyrite. However, the possibility that Tl, ‘loosely’ tied to the pyrite structure, could diffuse away during sample preparation and/or observation

should not be discarded, as it is well known that during ion milling there is non-negligible local heating of the sample (e.g., Barna et al., 1999), and that the highly focused electron beam required for EDS analysis may cause severe elemental diffusion (e.g., Capitani et al., 2016). Significant Tl levels were only detected in few thick grains in samples prepared by grinding. In this case, the greater thickness of the sample, and therefore the lower electron dose, may have prevented elemental diffusion. The drawback of this situation is that the thickness of the sample also prevents any microstructural information to be obtained.

The ‘loose’ nature of the Tl incorporation in pyrite is further confirmed by its expulsion under pyrite low-grade metamorphic recrystallization. As shown by George et al. (2018a), after recrystallization, pyrite from the ore deposits of southern Apuan Alps is depleted in As, Sb, Tl, Hg, Cu, Zn, Ag, and Mn, whereas Ni, Co, and As are sometimes even enriched. These results fully agree with those reported by Large et al. (2007, 2011), who suggested that trace elements occurring as nanoinclusions or that are ‘loosely’ held in the pyrite structure are readily expelled during metamorphism, whereas those elements replacing Fe or S in the crystal structure remain and even become enriched during metamorphic recrystallization.

At the present stage of investigation, Tl-hosting NPs have not been observed in pyrite. On the contrary, XAS data suggest its occurrence as a monovalent cation, with variable local environments, compatible with its occurrence in structural defects lacking long-range order. In conclusion, we confidently suggest that Tl could be present in the defective structure of pyrite.

5.1.3 Arsenic-rich “fluid” inclusions in pyrite

An interesting feature shown by HRTEM is the occurrence of As-rich “fluid” inclusions, similar to those observed by Deditius et al. (2009) who revealed As-enrichment in amorphous Fe-As-S nanoscale “liquid” inclusions in arsenian pyrite from Pueblo Viejo, Dominican Republic. There are two alternative ways to interpret the occurrence of these inclusions. Following Deditius et al. (2009), a possible interpretation is that these inclusions are primary features, trapped during the crystallization of host pyrite, in agreement with the observation of the precipitation of an amorphous Fe-As-S phase

via bacterial activity by some authors (e.g., Morin and Calas, 2006). On the contrary, taking into account the results reported by George et al. (2018a), these As-rich “liquid” inclusions could be sulphide melt nano-droplets exsolved during the final stages of the Apuan Alps metamorphism. According to Deditius and Reich (2016), these kinds of nanoparticles may be able to sequester migrating/diffusing elements, like, for instance, Tl. It is worth noting that Guillemin et al. (1970) reported the occurrence of an amorphous $\text{Tl}(\text{As,Sb})_{10}\text{S}_{16}$ phase in the Jas Roux deposit, Hautes-Alpes, France.

5.2 Environmental implications

The confirmation that Tl is present in the monovalent state in pyrite has significant environmental implications. Xiong (2009) calculated that Tl^+ is the dominant Tl species over geochemically reasonable pH ranges for soils. Similarly, Vink (1993) showed that Tl^+ is the most stable state of Tl under ‘normal’ Eh-pH conditions. Monovalent Tl is very mobile in the environment, being easily transported in aqueous form due to its high solubility (e.g., Vink, 1993; Peter and Viraraghavan, 2005). In a study of the toxicity and availability of both monovalent and trivalent Tl, Ralph and Twiss (2002) showed that, though Tl^{3+} is likely orders of magnitude more toxic than Tl^+ to algae, concentrations of available Tl^{3+} , even in polluted environments, are far below dangerous toxicity levels. This is because Tl^{3+} is largely locked within $\text{Tl}(\text{OH})_3$ under near-neutral pH conditions. On the contrary, the bioavailable fraction of Tl^+ is approximately equal to the total amount of dissolved Tl^+ in water. Thus, Tl^+ is far more of an environmental concern than Tl^{3+} .

Given the stability of Tl^+ in the environment, as well as its high mobility in this state, the release of Tl^+ from pyrite will lead to its uninhibited movement into the environment. Under normal Eh-pH conditions, free Tl^+ may readily be transported in ground or surface waters and dispersed. Importantly, Tl in the monovalent state is readily bioavailable; no chemical transformation is thus necessary, after release from pyrite, before Tl can be transported and made available for uptake into biota. The thallium contamination related to the ore deposits of southern Apuan Alps is an interesting case study (e.g., Biagioni et al., 2017). Given that, historically, Tl has not been as economically

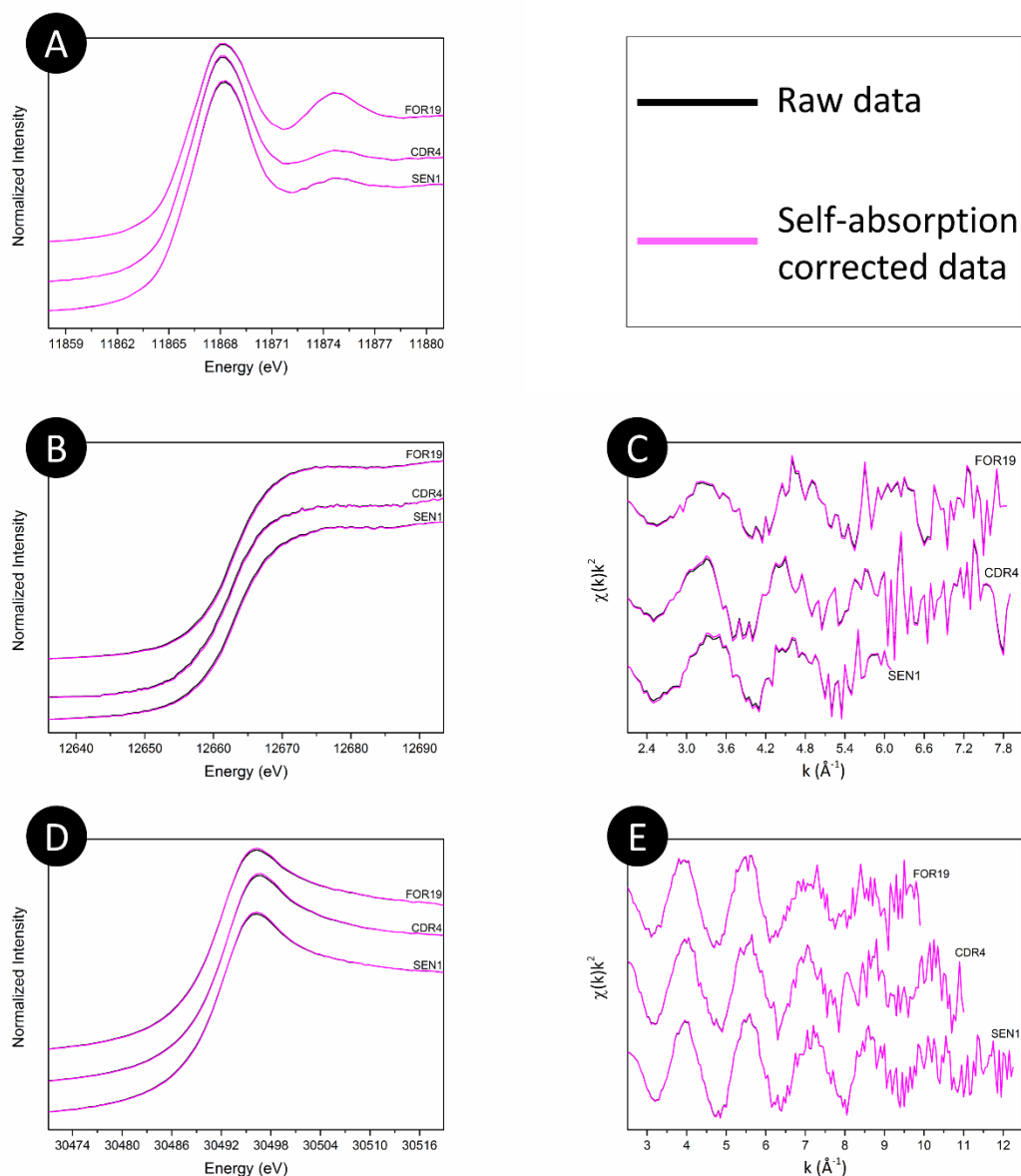
valuable as many other trace metals present in sulphide ores, it has rarely been recovered during the processing of such ores (Zitko et al., 1975). As such, Tl-bearing pyrite would be frequently discarded with ore tailings. Therefore, the oxidation of pyrite contained in mine dumps and tailings in Tl-rich mining areas worldwide potentially represents a severe environmental hazard.

Acknowledgements

This research received support from Ministero dell'Istruzione, dell'Università e della Ricerca through the project SIR 2014 "THALMIGEN – Thallium: Mineralogy, Geochemistry, and Environmental Hazards", granted to CB (Grant no. RBSI14A1CV). The critical reading and the suggestions of Yves Moëlo were greatly appreciated. The paper benefited of the comments and suggestions of two anonymous reviewers.

Declaration of Interest: None

Appendix A



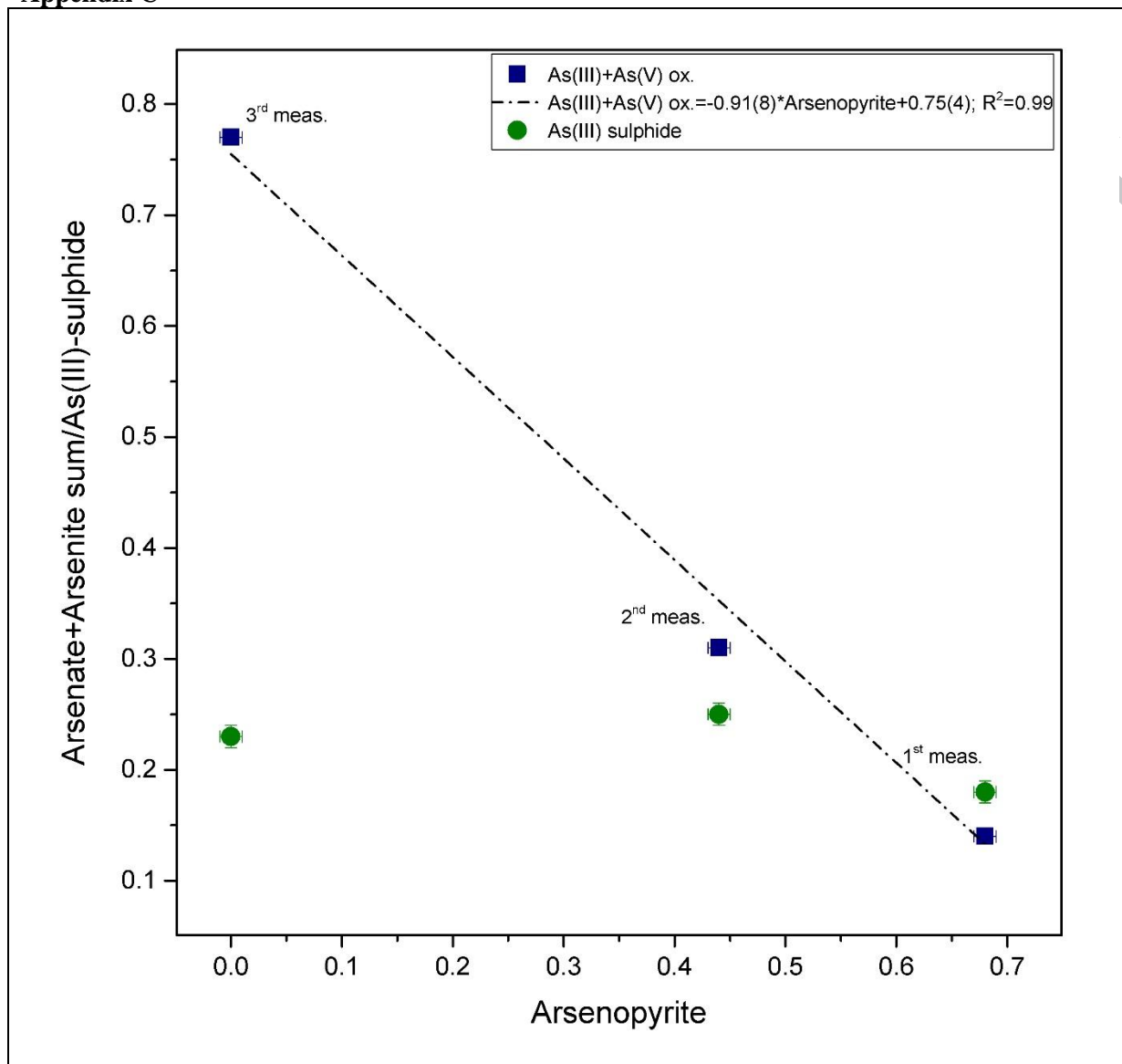
Comparison between raw and self-absorption corrected data on the XANES (left) and EXAFS (right) regions of collected spectra. Corrections were run at all absorption edges using the ATHENA software. A) XANES region at As *K*-edge; B) XANES region at Tl *L*₃-edge; C) Tl *L*₃-edge EXAFS region; D) XANES region at Sb *K*-edge; E) Sb *K*-edge EXAFS region.

Appendix B. Ga₂O₃ filter transmissivity at selected energies

	Transmissivity (%)
Fe <i>K</i> α ₁ = 6405.2 eV	7
Tl <i>L</i> α ₁ = 10,269 eV	50
As <i>K</i> α ₁ = 10,543 eV	4

Calculations were made using the Xpower tool, included in the XOP package (del Rio and Dejus, 1998).

Appendix C



Relative proportions of As phases as obtained from LCF analysis on three consecutive measurements on sample FOR19.

References

- Abratis P.K., Patrick R.A.D. and Vaughan D.J. (2004) Variations in compositional, textural and electrical properties of natural pyrite: a review. *Int. J. Mineral. Proc.* **74**, 41-59.

- Agarwal A. and Vishnoi A. N. (2005) XANES studies of thallium compounds and valence states and local environment of thallium in some of its superconducting cuprates. *Phys. Scr.* **T115**, 534-537.
- Ankudinov A. L., Ravel B., Rehr J. J. and Conradson S. D. (1998) Real-space multiple-scattering calculation and interpretation of X-ray-absorption near-edge structure. *Phys. Rev. B* **58**, 7565-7576.
- Balić-Žunić T. and Engel P. (1983) Crystal structure of synthetic $\text{PbTlAs}_3\text{S}_6$. *Z. Kristallogr. Cryst. Mater.* **165**, 261-270.
- Balić-Žunić T., Karanović L. and Poleti D. (2008) Crystal Structure of Picotpaulite, TlFe_2S_3 , from Allchar, FYR Macedonia. *Acta Chim. Slov.* **55**, 801-809.
- Barna A., Pécz B. and Menyhard M. (1999) TEM sample preparation by ion milling/amorphization. *Micron* **30**, 267-276.
- Batley G. E. and Florence T. M. (1975) Determination of thallium in natural waters by anodic stripping voltammetry. *J. Electroanal. Chem.* **61**, 205-211.
- Belousov I. A., Danyushevsky L. V., Olin P. H., Gilbert S. E. and Thompson J. (2015) STDGL3 - a new calibration standard for sulphide analysis by LA-ICP-MS. *Goldschmidt Abstracts* **2015**, 251.
- Berger R. (1989) Synthesis and characterization of the layered metal TlCu_2S_2 . *J. Less Common Met.* **147**, 141-148.
- Berlepsch P. (1996) Crystal structure and crystal chemistry of the homeotypes edenharterite ($\text{TlPbAs}_3\text{S}_6$) and jentschite ($\text{TlPbAs}_2\text{SbS}_6$) from Lengenbach, Binntal (Switzerland). *Schweiz. Mineral. Petrogr. Mitt.* **76**, 147-157.
- Biagioni C., D'Orazio M., Vezzoni S., Dini A. and Orlandi P. (2013) Mobilization of Tl-Hg-As-Sb-(Ag,Cu)-Pb sulfosalt melts during low-grade metamorphism in the Alpi Apuane (Tuscany, Italy). *Geology* **41**, 747-750.
- Biagioni C., Bonaccorsi E., Moëlo Y., Orlandi P., Bindi L., D'Orazio M. and Vezzoni S. (2014) Mercury-arsenic sulfosalts from the Apuan Alps (Tuscany, Italy). II. Arsiccioite, $\text{AgHg}_2\text{TlAs}_2\text{S}_6$, a new mineral from the Monte Arsiccio mine: occurrence, crystal structure and crystal chemistry of the routhierite isotopic series. *Mineral. Mag.* **78**, 101-117.
- Biagioni C., D'Orazio M., Lepore G. O., d'Acapito F. and Vezzoni S. (2017) Thallium-rich rust scales in drinkable water distribution systems: A case study from northern Tuscany, Italy. *Sci. Total Environ.* **587**, 491-501.

- Bindi L., Nestola F., Makovicky E., Guastoni A. and De Battisti L. (2014) Tl-bearing sulfosalt from the Lengnabach quarry, Binn valley, Switzerland: Philrothite, TlAs_3S_5 . *Mineral. Mag.* **78**, 1-9.
- Booth, C. H., & Bridges, F. (2005). Improved self-absorption correction for fluorescence measurements of extended X-ray absorption fine-structure. *Phys. Scr.* **T115**, 202-204.
- Brese, N.E. and O'Keeffe, M. (1991) Bond-valence parameters for solids. *Acta Crystallogr.*, **B47**, 192-197.
- Brown, I. D. and Altermatt, D. (1985) Bond-valence parameters obtained from a systematic analysis of the Inorganic Crystal Structure Database. *Acta Crystallogr.* **B41**, 244-247.
- Brown K. L. and Dickson F. W. (1976) The crystal structure of synthetic christite, HgTlAsS_3 . *Z. Kristallogr.* **144**, 367-376.
- Capitani G.C., Schingaro M., Lacalamita M., Mesto E. and Scordari F. (2016) Structural anomalies in tobelite- $2M_2$ explained by high resolution and analytical electron microscopy. *Mineral. Mag.*, **80**, 143-156.
- Cook N. J., Ciobanu C. L., Pring A., Skinner W., Shimizu M., Danyushevsky L., Saini-Eidukat B. and Melcher F. (2009) Trace and minor elements in sphalerite: A LA-ICPMS study. *Geochim. Cosmochim. Acta* **73**, 4761-4791.
- d'Acapito F, Trapananti A, Torrenzo S. and Mobilio S. (2014) X-ray absorption spectroscopy: the Italian Beamline GILDA at the ESRF. *Not. Neutron. Luce di Sincrotrone* **19**, 14-23.
- d'Acapito, F.; Lepore, G.O.; Puri, A.; Laloni, A.; La Mannna, F.; Dettona, E.; De Luisa, A.; Martin, A. (2019) The LISA beamline at ESRF. *J. Synchrotron Radiat.* **26**, (in press), <https://doi.org/10.1107/S160057751801843X>.
- D'Orazio M., Biagioni C., Dini A. and Vezzoni S. (2017) Thallium-rich pyrite ores from the Apuan Alps, Tuscany, Italy: constraints for their origin and environmental concerns. *Mineral. Depos.* **52**, 687-707.
- Deditius A. P. and Reich M. (2016) Constraints on the solid solubility of Hg, Tl, and Cd in arsenian pyrite. *Am. Mineral.* **101**, 1451-1459.
- Deditius A. P., Utsunomiya S., Renock D., Ewing R. C., Ramana C. V., Becker U. and Kesler S. E. (2008) A proposed new type of arsenian pyrite: composition, nanostructure and geological significance. *Geochim. Cosmochim. Acta* **72**, 2919-2933.
- Deditius A.P., Utsunomiya S., Ewing R.C. and Kesler S.E. (2009) Nanoscale "liquid" inclusions of As-Fe-S in arsenian pyrite. *Am. Mineral.* **94**, 391-394.
- Deditius A.P., Utsunomiya S., Kesler S.E., Reich M. and Ewing R.C. (2011) Trace elements nanoparticles in pyrite. *Ore Geol. Rev.* **42**, 32-46.

- Deditius A.P., Reich M., Kesler S.E., Utsunomiya S., Chryssoulis S.L., Walshe J. and Ewing R.C. (2014) The coupled geochemistry of Au and As in pyrite from hydrothermal ore deposits. *Geochim. Cosmoch. Acta* **140**, 644-670.
- Dutrizac J. E., Chen T. T. and Beauchemin S. (2005) The behaviour of thallium (III) during jarosite precipitation. *Hydrometallurgy* **79**, 138-153.
- Engel P. (1980) Die Kristallstruktur von synthetischem Parapierrrotit, TlSb_5S_2 . *Z. Kristallogr. Cryst. Mater.* **151**, 203-230.
- Engel P., Nowacki W., Balić-Žunić T. and Šćavničar S. (1982) The crystal structure of simonite, $\text{TlHgAs}_3\text{S}_6$. *Z. Kristallogr. Cryst. Mater.* **161**, 159-166.
- Engel P., Gostojić M. and Nowacki W. (1983) The crystal structure of pierrotite, $\text{Tl}_2(\text{Sb,As})_{10}\text{S}_{16}$. *Z. Kristallogr. Cryst. Mater.* **165**, 209-216.
- Erwin S.C., Zu L., Haftel M.I. Efron A.L., Kennedy T.A. and Norris D.J. (2005) Doping semiconductor nanocrystals. *Nature* **436**, 91-94.
- Fellin M.G., Reiners P.W., Brandon M.T., Wüthrich E., Balestrieri M.L. and Molli G. (2007) Thermochronologic evidence for exhumational history of the Alpi Apuane metamorphic core complex, northern Apennines, Italy. *Tectonics* **26**, doi: 10.1029/2006TC002085.
- Fleet M. E. (1973) The crystal structure and bonding of lorandite, $\text{Tl}_2\text{As}_2\text{S}_4$. *Z. Kristallogr. Cryst. Mater.* **138**, 147-160.
- George L., Cook N. J., Cristiana L. and Wade B. P. (2015) Trace and minor elements in galena: A reconnaissance LA-ICP-MS study. *Am. Mineral.* **100**, 548-569.
- George L. L., Biagioni C., D'Orazio M., Cook N. J. (2018a) Textural and trace element evolution of pyrite during greenschist facies metamorphic recrystallization in the southern Apuan Alps (Tuscany, Italy): initiation of Tl-rich sulphosalt melt formation. *Ore Geol. Rev.* **102**, 59-105.
- George L. L., Cook N. J., Crowe B. B. P. and Ciobanu C. L. (2018b) Trace elements in hydrothermal chalcopyrite. *Mineral. Mag.* **82**, 59-88.
- Giester G., Lengauer C. L., Tillmanns E. and Zemann J. (2002) Tl_2S : Re-determination of crystal structure and stereochemical discussion. *J. Solid State Chem.* **168**, 322-330.
- Gostojić M. (1980) Die Kristallstruktur von synthetischem ellisit, Tl_3AsS_3 . *Z. Kristallogr. Cryst. Mater.* **151**, 249-254.

- Gostojić M., Edenharter A., Nowacki W. and Engel P. (1982) The crystal structure of synthetic $Tl_2MnAs_2S_5$. *Z. Kristallogr. Cryst. Mater.* **158**, 43-52.
- Graeser S., Berlepsch P., Makovicky E. and Balic-Zunic T. (2001) Sicherite, $TlAg_2(As,Sb)_3S_6$, a new sulfosalt mineral from Lengnabach (Binntal, Switzerland): Description and structure determination. *Am. Mineral.* **86**, 1087-1093.
- Guillemin C., Johan Z., Laforêt C. and Picot P. (1970) La pierrotite, $Tl_2(Sb,As)_{10}S_{17}$, une nouvelle espèce minérale. *Bull. Soc. Fr. Mineral. Cristallogr.* **93**, 66-71.
- Huston D. L., Sie S. H., Suter G. F., Cooke D. R. and Both R. A. (1995) Trace elements in sulfide minerals from eastern Australian volcanic-hosted massive sulfide deposits; Part I, Proton microprobe analyses of pyrite, chalcopyrite, and sphalerite, and Part II, Selenium levels in pyrite; comparison with delta 34 S values and implications for the source of sulfur in volcanogenic hydrothermal systems. *Econ. Geol.* **90**, 1167-1196.
- Karbowska B. (2016) Presence of thallium in the environment: sources of contaminations, distribution and monitoring methods. *Environ. Monit. Assess.* **188**, 640.
- Karlsson U., Karlsson S. and Düker A. (2006) The effect of light and iron(II)/iron(III) on the distribution of Tl(I)/Tl(III) in fresh water systems. *J. Environ. Monit.* **8**, 634-640.
- Keith L. H. and Telliard W. A. (1979) Priority pollutants-I. A perspective view. *Environ. Sci. Technol.* **13**, 416-423.
- Kilaas R. (1998) Optimal and near-optimal filters in high-resolution electron microscopy. *J. Microsc.* **190**, 45-51.
- Kouzmanov K., Pettke T. and Heinrich C.A. (2010) Direct analysis of ore-precipitating fluids: Combined IR microscopy and LA-ICP-MS study of fluid inclusions in opaque ore minerals. *Econ. Geol.* **105**, 351-373.
- Large R.R., Maslennikov V.V., Robert F., Danyushevsky L.V. and Chang Z. (2007) Multistage sedimentary and metamorphic origin of pyrite and gold in the Giant Sukoilog deposit, Lena Gold Province, Russia. *Econ. Geol.* **102**, 1233-1267.
- Large R.R., Bull S.W. and Maslennikov V.V. (2011) A carbonaceous sedimentary source-rock model for carlin-type and orogenic gold deposits. *Econ. Geol.* **106**, 331-358.
- Laznicka P. (2010) Giant metallic deposits: Future sources of industrial metals. Second edition. Springer-Verlag Berlin Heidelberg.

- Lee P. A., Citrin P. H., Eisenberger P. T. and Kincaid B. M. (1981) Extended X-ray absorption fine structure - its strengths and limitations as a structural tool. *Rev. Mod. Phys.* **53**, 769-806.
- Makovicky E. (2018) Modular crystal chemistry of thallium sulfosalts. *Minerals* **8**, 478.
- Mitchell D.R. (2007) HRTEM filter. Digital_Micrograph_Script_Database. http://felmpc14.tugraz.ac.at/dm_scripts/freeware/programs/hrtem_filter.htm.
- Morin G. and Calas G. (2006) Arsenic in soils, mine tailings, and former industrial sites. *Elements* **2**, 97-101.
- Nriagu J. O. (1998) Thallium in the Environment. John Wiley & Sons Inc., New York
- Ohmasa M. and Nowacki W. (1971) The crystal structure of vrbaitite $\text{Hg}_3\text{Tl}_4\text{As}_8\text{Sb}_2\text{S}_{20}$. *Z. Kristallogr. Cryst. Mater.* **134**, 360-380.
- Orlandi P., Biagioni C., Bonaccorsi E., Moëlo Y. and Paar W. (2012) Lead-antimony sulfosalts from Tuscany (Italy). XII. Boscardinite, $\text{TlPb}_4(\text{Sb}_7\text{As}_2)_{\Sigma 9}\text{S}_{18}$, a new mineral species from the Monte Arsiccio mine: occurrence and crystal structure. *Can. Mineral.* **50**, 235-251.
- Orlandi P., Biagioni C., Moëlo Y., Bonaccorsi E. and Paar W. (2013) Lead-antimony sulfosalts from Tuscany (Italy). XIII. Protochabournéite, $\sim\text{Tl}_2\text{Pb}(\text{Sb}_{9.8}\text{As}_{1.2})_{\Sigma 10}\text{S}_{17}$, from the Monte Arsiccio mine: occurrence, crystal structure and relationship with chabournéite. *Can. Mineral.* **51**, 475-494.
- Pasava J., Pertlik F., Stumpfl E. F. and Zeman J. (1989) Bernardite, a new thallium arsenic sulphosalt from Allchar, Macedonia, with a determination of the crystal structure. *Mineral. Mag.* **53**, 531-538.
- Paton C., Hellstrom J., Paul B., Woodhead J. and Hergt J. (2011) Iolite: Freeware for the visualisation and processing of mass spectrometric data. *J. Anal. Atom. Spectrom.* **26**, 2508-2518.
- Peacock C. L. and Moon E. M. (2012) Oxidative scavenging of thallium by birnessite: explanation for thallium enrichment and stable isotope fractionation in marine ferromanganese precipitates. *Geochim. Cosmochim. Acta* **84**, 297-313.
- Peter A. L. J. and Viraraghavan T. (2005) Thallium: a review of public health and environmental concerns. *Environ. Int.* **31**, 439-501.
- Puri, A., Lepore, G. O., & d'Acapito, F. (2019). The New Beamline LISA at ESRF: Performances and Perspectives for Earth and Environmental Sciences. *Condens. Matter* **4**, 12.
- Qian G., Brugger J., Testamale D., Skinner W. and Pring A. (2013) Formation of As(II)-pyrite during experimental replacement of magnetite under hydrothermal conditions. *Geochim. Cosmochim. Acta* **100**, 1-10.

- Ralph L. and Twiss M. R. (2002) Comparative toxicity of thallium (I), thallium (III), and cadmium (II) to the unicellular alga *Chlorella* isolated from Lake Erie. *B. Environ. Contam. Tox.* **68**, 261-268.
- Ravel B. (2001) ATOMS: crystallography for the X-ray absorption spectroscopist. *J. Synchrotron Rad.* **8**, 314-316.
- Ravel B. and Newville M. (2005) ATHENA, ARTEMIS, HEPHAESTUS: data analysis for X-ray absorption spectroscopy using IFEFFIT. *J. Synchrotron Rad.* **12**, 537-541.
- Reich M., Kesler S. E., Utsunomiya S., Palenik C. S., Chryssoulis S. L. and Ewing R. C. (2005) Solubility of gold in arsenian pyrite. *Geochim. Cosmochim. Acta* **69**, 2781-2796.
- Reich M., Deditius A. P., Chryssoulis S., Li J. W., Ma C. Q., Parada M. A., Barra F. and Mittermayr F. (2013) Pyrite as a record of hydrothermal fluid evolution in a porphyry copper system: A SIMS/EMPA trace element study. *Geochim. Cosmochim. Acta* **104**, 42-62.
- Rey N., Jumas J. C., Olivier-Fourcade J. and Philippot E. (1983) Sur les composés III–V–VI: étude structurale du disulfure d'antimoine et de thallium, TlSbS_2 . *Acta Crystallogr. C Cryst. Struct. Comm.* **39**, 971-974.
- Rieder M., Crelling J.C., Sustai O., Drabek M., Weiss Z. and Klementova M. (2007) Arsenic in iron disulfides in a brown coal from the North Bohemian Basin, Czech Republic. *Int. J. Coal Geol.* **71**, 115-121.
- Sabrowsky H., Mirza J. and Methfessel C. (1979) Neue Phasen im System Thallium-Eisen-Schwefel/New Phases in the System Thallium-Iron-Sulphur. *Z. Naturforsch. B* **34**, 115.
- Savage K. S., Tingle T. N., O'Day P. A., Waychunas G. A. and Bird D. K. (2000) Arsenic speciation in pyrite and secondary weathering phases, Mother Lode gold district, Tuolumne County, California. *Appl. Geochem.* **15**, 1219-1244.
- Scheckel K. G., Lombi E., Rock S. A. and McLaughlin M. J. (2004) In vivo synchrotron study of thallium speciation and compartmentation in *Iberis intermedia*. *Environ. Sci. Technol.* **38**, 5095-5100.
- Shannon R.D. (1976) Revised effective ionic radii and systematic studies of interatomic distances in halides and chalcogenides. *Acta Crystallogr.* **A32**, 751-767.
- Simon G., Huang H., Penner-Hahn J. E., Kesler S. E. and Kao L. -S. (1999a) Oxidation state of gold and arsenic in gold-bearing arsenian pyrite. *Am. Mineral.* **84**, 1071-1079.
- Simon G., Kesler S. E. and Chryssoulis S. (1999b) Geochemistry and textures of gold-bearing arsenian pyrite, Twin Creeks, Nevada: implications for deposition of gold in Carlin-type deposits. *Econ. Geol.* **94**, 405-422.

- Van Cappellen E. and Doukhan J.D. (1994) Quantitative transmission X-ray microanalysis of ionic compounds. *Ultramicroscopy* **53**, 343-349.
- Vink B. W. (1993) The behaviour of thallium in the (sub) surface environment in terms of Eh and pH. *Chem. Geol.* **109**, 119-123.
- Wedepohl K. H. (1995) The composition of the continental crust. *Geochim. Cosmochim. Acta* **59**, 1217-1239.
- Welz D., Deppe P., Schaefer W., Sabrowsky H. and Rosenberg M. (1989) Magnetism of iron-sulfur tetrahedral frameworks in compounds with thallium I. Chain structures. *J. Phys. Chem. Solids* **50**, 297-308.
- Wilson J. R., Gupta P. K. S., Robinson P. D. and Criddle A. J. (1993) Fangite, Tl_3AsS_4 , a new thallium arsenic sulfosalt from the Mercur Au deposit, Utah, and revised optical data for gillulyite. *Am. Mineral.* **78**, 1096-1103.
- Xiong Y. (2007) Hydrothermal thallium mineralization up to 300 °C: a thermodynamic approach. *Ore Geol. Rev.* **32**, 291-313.
- Xiong Y. (2009) The aqueous geochemistry of thallium: speciation and solubility of thallium in low temperature systems. *Environ. Chem.* **6**, 441-451.
- Zelenski M., Garavelli A., Pinto D., Vurro F., Moëlo Y., Bindi L., Makovicky E. and Bonaccorsi E. (2009) Tazieffite, $Pb_{20}Cd_2(As,Bi)_{22}S_{50}Cl_{10}$, a new chloro-sulfosalt from Mutnovsky volcano, Kamchatka Peninsula, Russian Federation. *Am. Mineral.* **94**, 1312-1324.
- Zhou T. F., Fan Y., Yuan F., Wu M. A., Hou M. J., Voicu G., Hu Q. H., Zhang Q. M. and Yue S. C. (2005) A preliminary geological and geochemical study of the Xiangquan thallium deposit, eastern China: the world's first thallium-only mine. *Mineral. Petrol.* **85**, 243-251.
- Zitko V., Carson W. V. and Carson W. G. (1975) Thallium: occurrence in the environment and toxicity to fish. *B. Environ. Contam. Tox.* **13**, 23-30.

Figure captions

Figure 1

Textures shown by pyrite samples studied in this work. Samples are from Sennari (A, B), Canale della Radice (C, D), and Fornovolasco (E, F).

Figure 2

Representative LA-ICP-MS time-resolved down-hole ablation profiles from CDR4 (A), FOR19 (B) and (C), and SEN1 (D). Y axis = counts per second, X axis = time (s). Relatively flat spectra reflect solid solution or homogeneously distributed NPs. Reflected light images of the respective pyrite grains are also shown. Red dots indicate where the LA-ICP-MS spot was made (dot not to scale). LA-ICP-MS element map of Tl in colloform pyrite from FOR19 also shown in (B).

Figure 3

Plots showing inter-element correlations in pyrite. (A) Tl vs. Sb and (B) Tl vs. As. Data plotted as mol. %. Straight line is ideal 1:1 correlation.

Figure 4

Normalized Tl L_3 -edge XANES for measured samples and standards. The vertical dashed lines indicate the position of the main inflection point, which, by convention, is considered to be the absorption edge energy. It can be seen that all Tl^+ standard compounds have an absorption edge at ~ 12663 eV, while Tl_2O_3 at ~ 12669 eV.

Figure 5

(A) Tl L_3 -edge k^2 -weighted EXAFS region of measured samples. (B) Fourier transforms (uncorrected for phase shifts) of the EXAFS of measured samples. Solid lines are data, red lines are fits. Fits were performed in R space.

Figure 6

Coordination numbers (CNs) vs. Tl–S average bond distances for several Tl sulphide sites. Data from: Pasava et al., 1989 (bernardite); Giester et al., 2002 (carlinite); Ohmasa and Nowacki, 1971 (vrbaite); Brown and Dickson, 1976 (christite); Balić-Žunić and Engel, 1983 (edenharterite); Orlandi et al., 2013 (protochabournéite); Rey et al., 1983 (weissbergite); Engel, 1980 (parapierrotite); Berlepsch, 1996 (jentschite); Engel et al., 1982 (simonite); Balić-Žunić et al., 2008 (picotpaulite); Berger, 1989 (thalcusite); Fleet, 1973 (lorándite); Bindi et al., 2014 (philrothite); Graeser et al., 2001 (sicherite); Wilson et al., 1983 (fangite); Gostojić, 1980 (ellisite); Engel et al., 1983 (pierrotite).

Figure 7

Calibrated and normalized As K -edge XANES spectra of studied samples (black line) and measured reference compounds (black dotted line). Linear combination fit (LCF) of studied samples are shown in red. Vertical dashed lines in correspondence of the main inflection point of arsenopyrite (As^-), protochabournéite (As^{3+}) and adamite (As^{5+}).

Figure 8

Normalized Sb K -edge XANES for measured samples and standards. Vertical dashed lines in correspondence of the main inflection point of Sb_2O_3 , Sb_2S_3 and Sb_2O_5 .

Figure 9

(A) Sb K -edge k^2 -weighted EXAFS region of measured samples. (B) Fourier transforms (uncorrected for phase shifts) of the EXAFS of measured samples. Solid lines are data, red lines are fits. Fits were performed in R space.

Figure 10

Ion-milled sample CDR4. (A) BF image showing different dislocations whose contrast is due to different operating Burger vectors and to different orientations of dislocation lines. White arrows mark long and curved dislocations; black arrows show short and straight dislocations. (B) BF image showing a lamella (white arrow) and several straight dislocations. (C) HR image taken along $[0\bar{1}1]$ (SAED pattern shown in the inset) on two short and straight dislocations. (D) Enlargement of the square region in C (see text for details) showing HR image taken along $[0\bar{1}1]$ with (011) lattice planes offset by $\frac{1}{2}[011]$ from one side to the other of the dislocation line.

Figure 11

(A) BF images showing inclusions with polygonal shape (some them indicated by arrows) of the ion-milled sample CDR4. (B) HRTEM images taken along $[0\bar{1}1]$ (related SAED pattern in the inset) of the ion-milled sample CDR4. The polygonal shape of the inclusion in the HR image is determined by pyrite crystallographic planes (indexed).

Figure 12

(A) EDS spectrum of fluid inclusions showing As-enrichment. (B) EDS spectrum of thick area from the ground FOR19 sample, exhibiting Tl and Sb. Nickel, Cu and Cr peaks are due to grid.

Table 1. Summary of trace element concentrations in pyrite determined by LA-ICP-MS (data in ppm).

Deposit	Sample		Mn	Co	Ni	Cu	Zn	As	Se	Mo	Ag	Cd	In	Sn	Sb
Sennari	SEN1	Mean	14	14	151	10	20	364	1.0	18	0.74	0.7	0.002	0.06	1299
		St. Dev.	12	29	196	7.5	20	269	0.73	22	0.78	0.7	0.001	0.03	1382
Canale della Radice	CDR4	Mean	80	60	836	90	65	1857	3.3	41	0.92	0.8	0.02	0.69	1871
		St. Dev.	87	74	1047	89	85	988	4.7	59	1.1	1.1	0.03	1.64	1156
Fornovolasco	FOR19	Mean	35	5.9	88	8.5	40	1602	5.3	45	2.4	0.3	0.00	<MDL	1896
		St. Dev.	22	5.7	70	6.3	20	892	6.7	26	1.7	0.2	0.00	-	914

MDL = Minimum Detection Limi

Table 2. EXAFS multiparameter fit details for Tl L_3 -edge

	Path	CN	R (Å)	σ^2 (Å ²)	k range (Å ⁻¹)
SEN1	Tl-S	5(2)	3.16(5)	0.03(1)	2.6-5.3
FOR19	Tl-S	2.1(3)	2.98(2)	0.013(3)	2.6-7.4
CDR4	Tl-S	6(1)	3.21(2)	0.036(4)	2.4-6.4
Protochabournéite	Tl-S _I	6(1)	3.25(2)	0.014(1)	2.4-8.3
	Tl-S _{II}	3(1)	3.50(2)	//	//

CN = coordination number. R = path length. σ^2 = Debye-Waller factor. Errors, as calculated by ARTEMIS, are indicated in parentheses.

Table 3. Relative weight of As species from linear combination fit (LCF) of pyrite samples (As *K*-edge).

	Protochabournéite (As ³⁺ sulfide)	Arsenopyrite (As ⁻¹)	Adamite (As ⁵⁺ , arsenate)	R factor ($\Sigma(\text{data-fit})^2/\Sigma(\text{data})^2$)
SEN1	0.35(1)	0.58(1)	0.07(1)	0.0002
CDR4	0.30(1)	0.63(1)	0.07(1)	0.0002
FOR19	0.18(1)	0.67(1)	0.14(1)	0.0001

All measured As standards were used for the fit allowing a maximum number of 4 standards for each fit; relative weights were constrained to be positive and to sum to 1. Results for sample FOR19 are relative to the sole first measurement. Errors in parentheses are 1-sigma errors generated in ATHENA.

Table 4. EXAFS multiparameter fit details for Sb *K*-edge

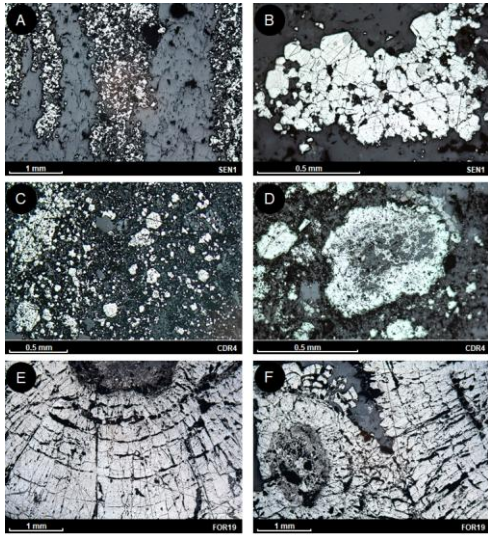
	Path	CN	R (Å)	σ^2 (Å ²)	<i>k</i> range (Å ⁻¹)
SEN1	Sb-S	2.4(2)	2.498(8)	0.005(1)	3.3-10.5
FOR19	Sb-S	3.0(4)	2.53(1)	0.012(2)	3.3-8.8
CDR4	Sb-S	2.4(5)	2.52(2)	0.008(2)	3.3-10.5
Sb₂S₃	Sb-S	0.80(5)	2.515(5)	0.0088(7)	3.3-11.7
	//	1.6(1)	2.535(5)	//	//
	Sb-Sb	3.2(2)	3.826(8)	0.018(2)	//
Sb₂O₃	Sb-O	4.9(5)	2.218(7)	0.003(1)	3.3-12.3
	Sb-Sb	1.9(2)	3.38(1)	0.006(1)	//
	//	0.97(9)	3.66(1)	//	//
	//	//	3.72(1)	//	//
	//	1.9(2)	3.92(1)	//	//
	//	//	4.06(1)	//	//

CN = coordination number. R = path length. σ^2 = Debye-Waller factor. Errors, as calculated by ARTEMIS, are indicated in parentheses. The reported Sb-O first shell for Sb₂O₃ represents the average of five Sb-O paths with Sb-O distances ranging from 1.97 to 2.60 Å.

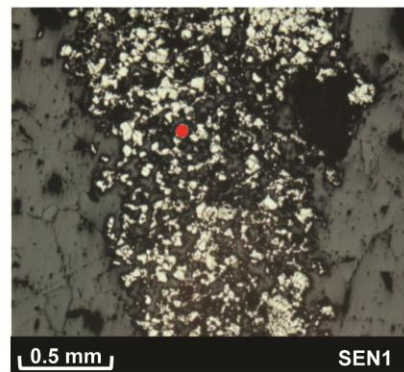
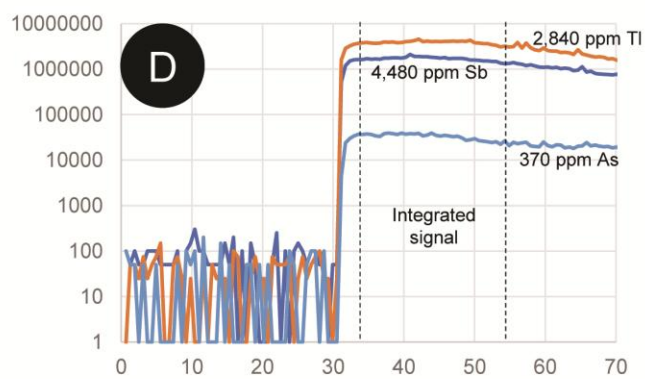
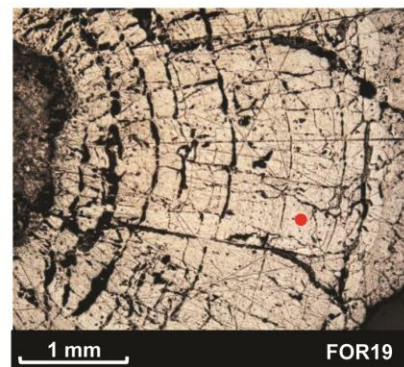
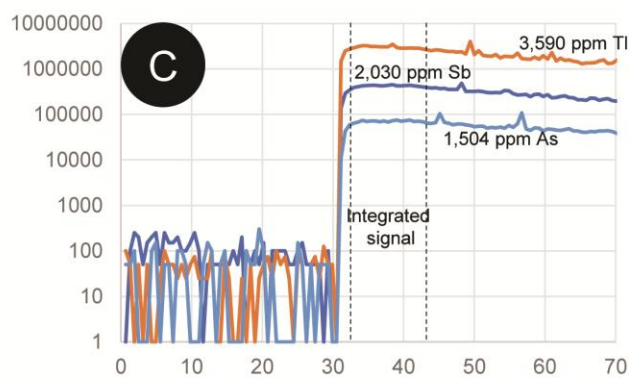
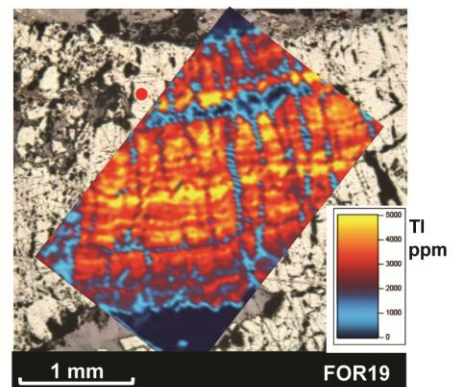
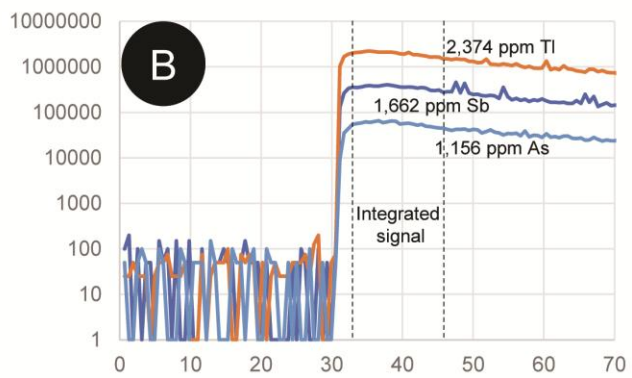
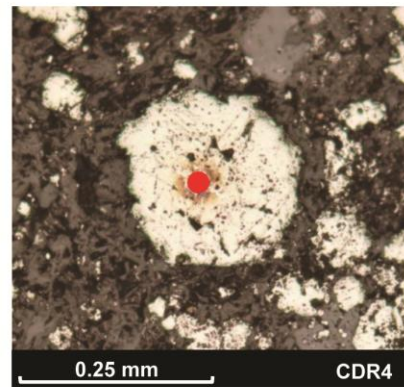
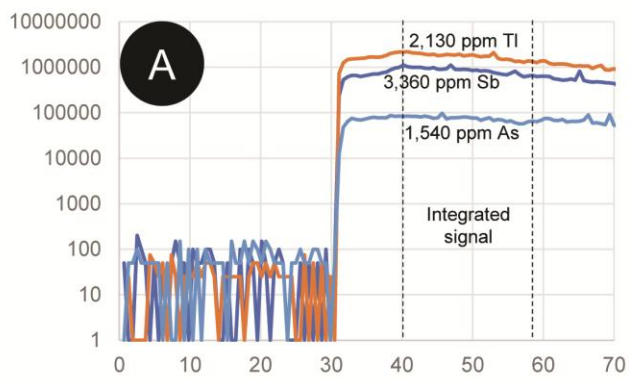
Highlights:

- Thallium is hosted as Tl^+ with Sb^{3+} , As^{3+} , and As^{1-} in (Tl,Sb,As)-rich pyrite
- Thallium likely occurs in pyrite structural defects lacking any long-range order
- The release of loosely bound Tl from pyrite is a potential environmental hazard

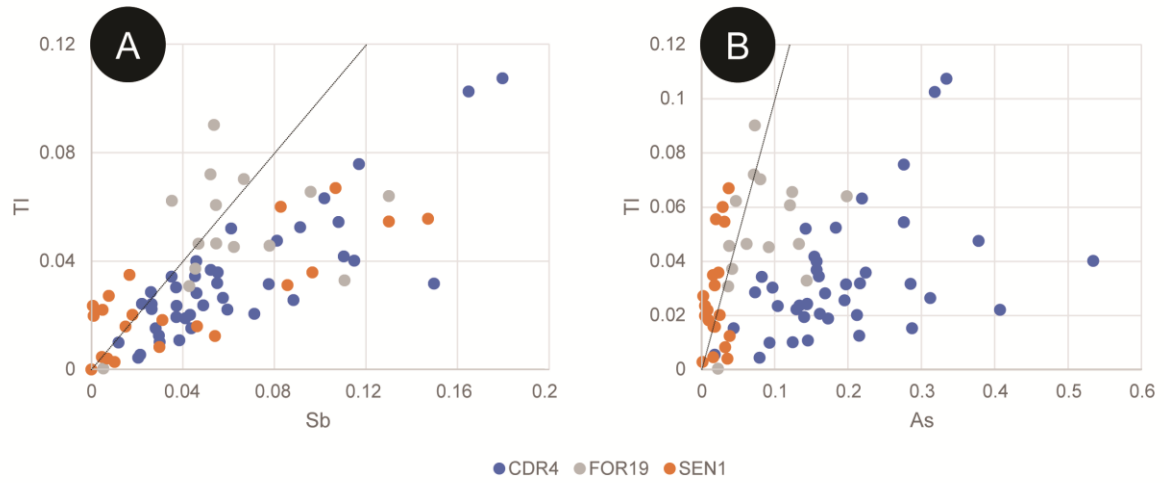
ACCEPTED MANUSCRIPT



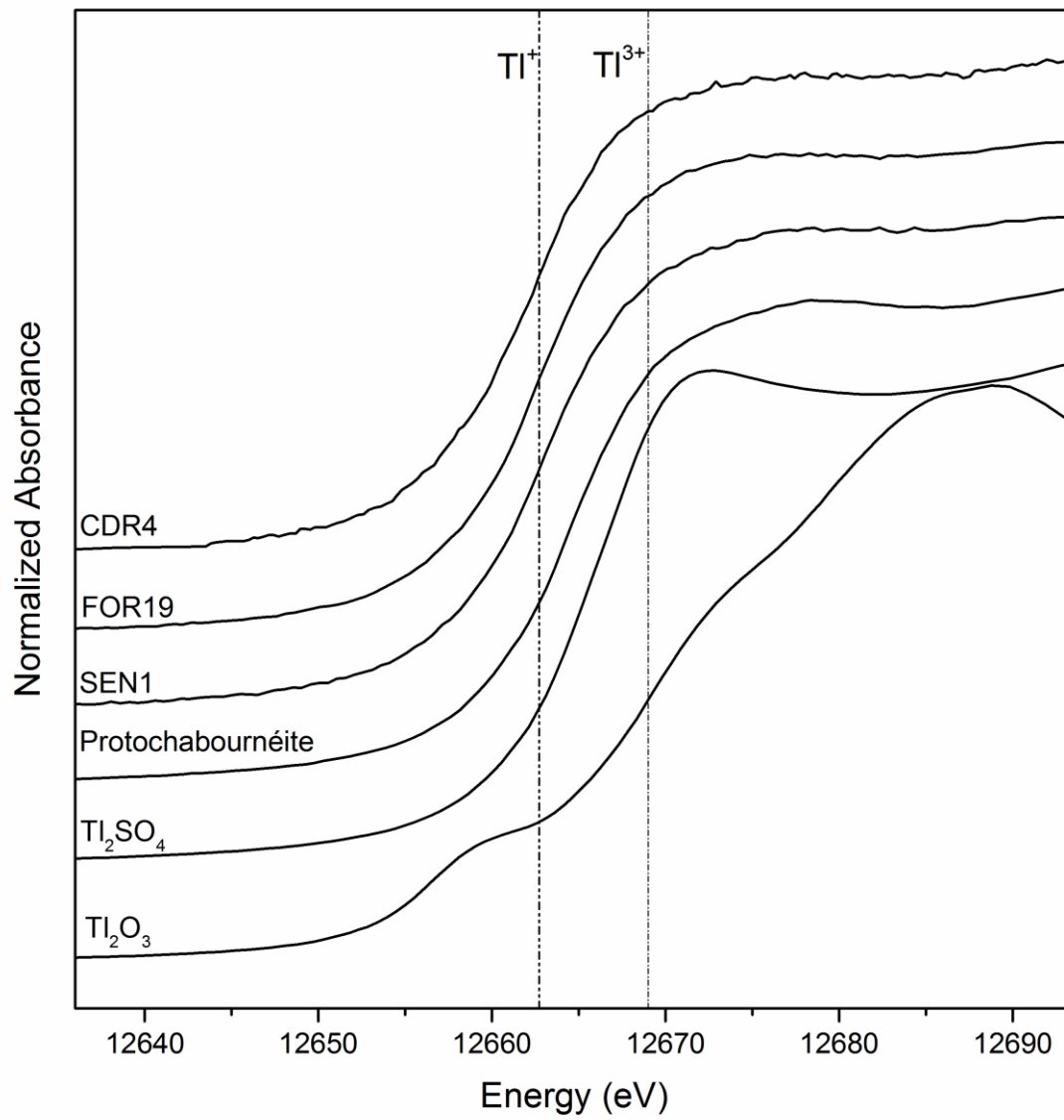
ACCEPTED MANUSCRIPT



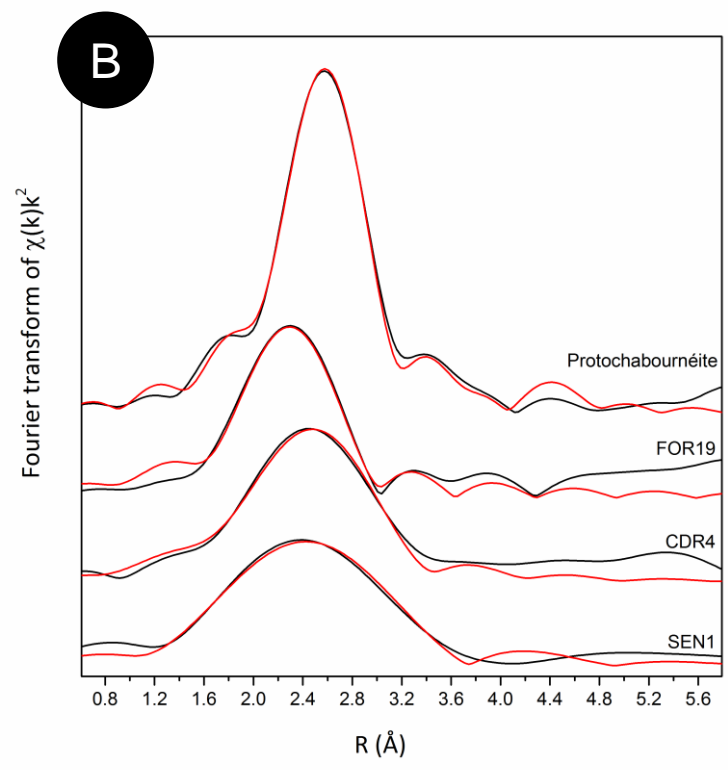
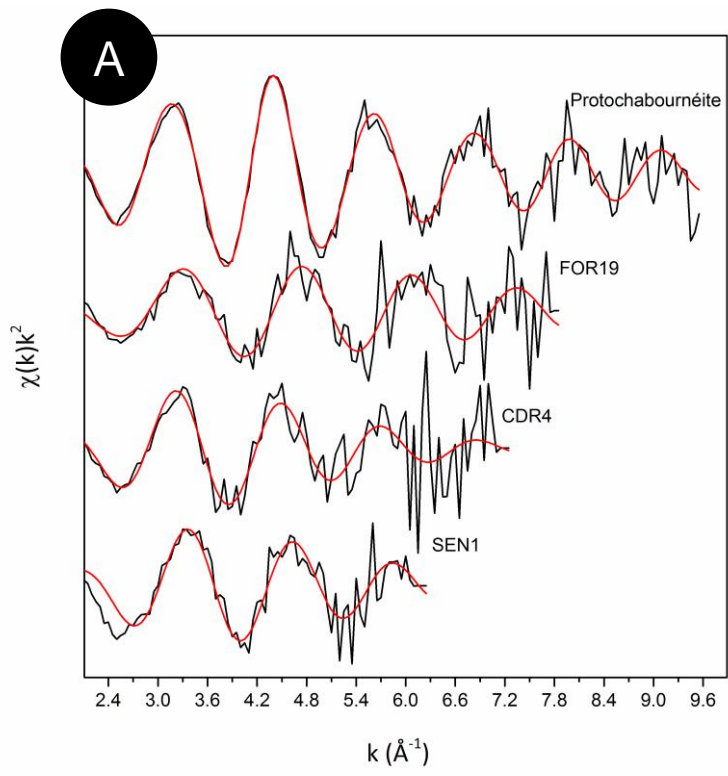
— Sb — Tl — As

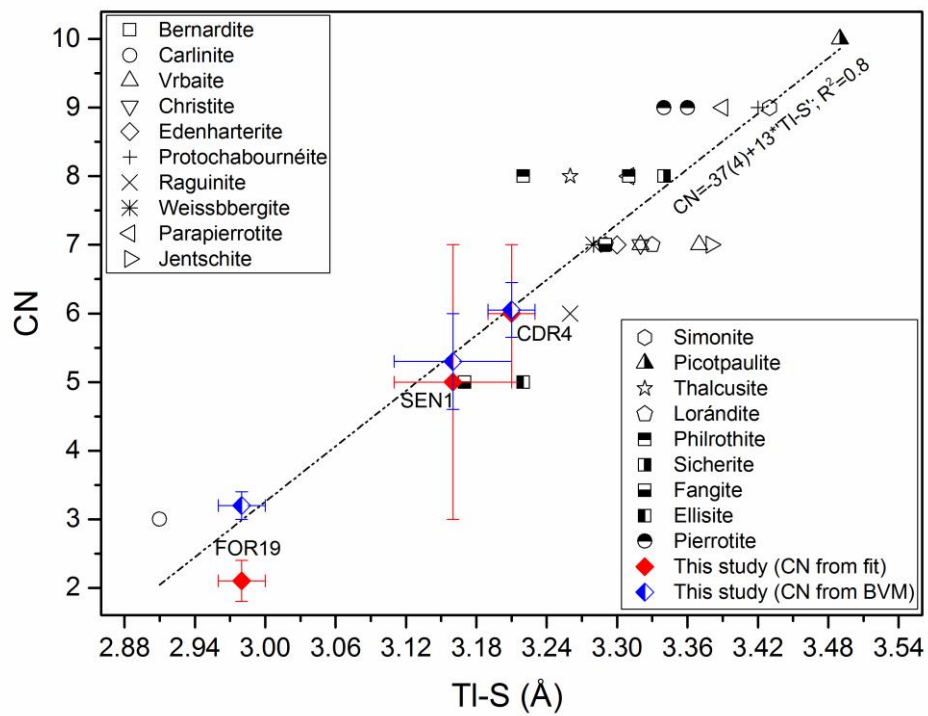


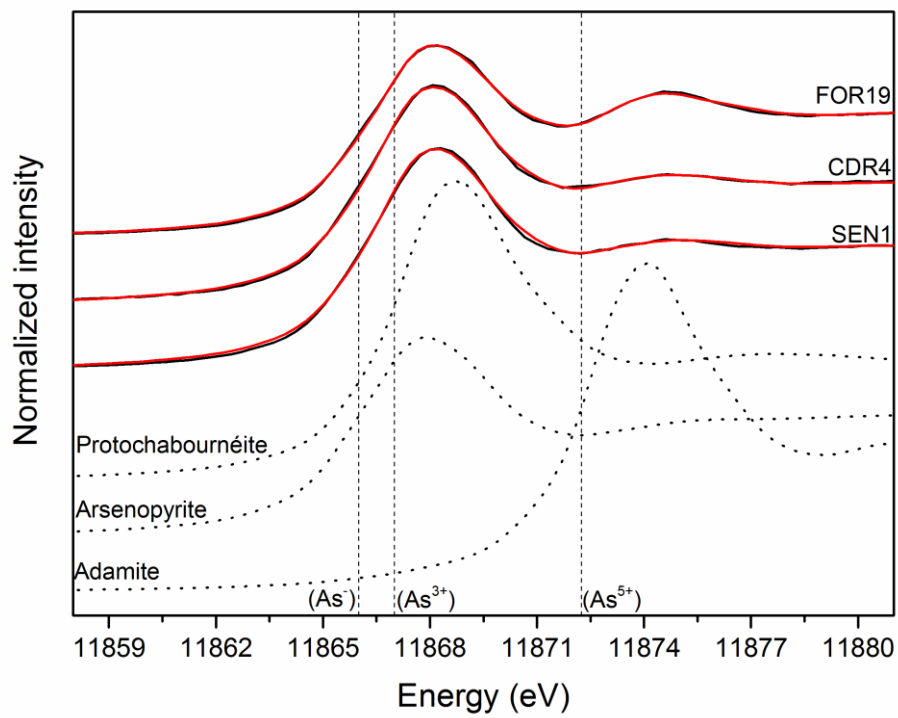
ACCEPTED MANUSCRIPT



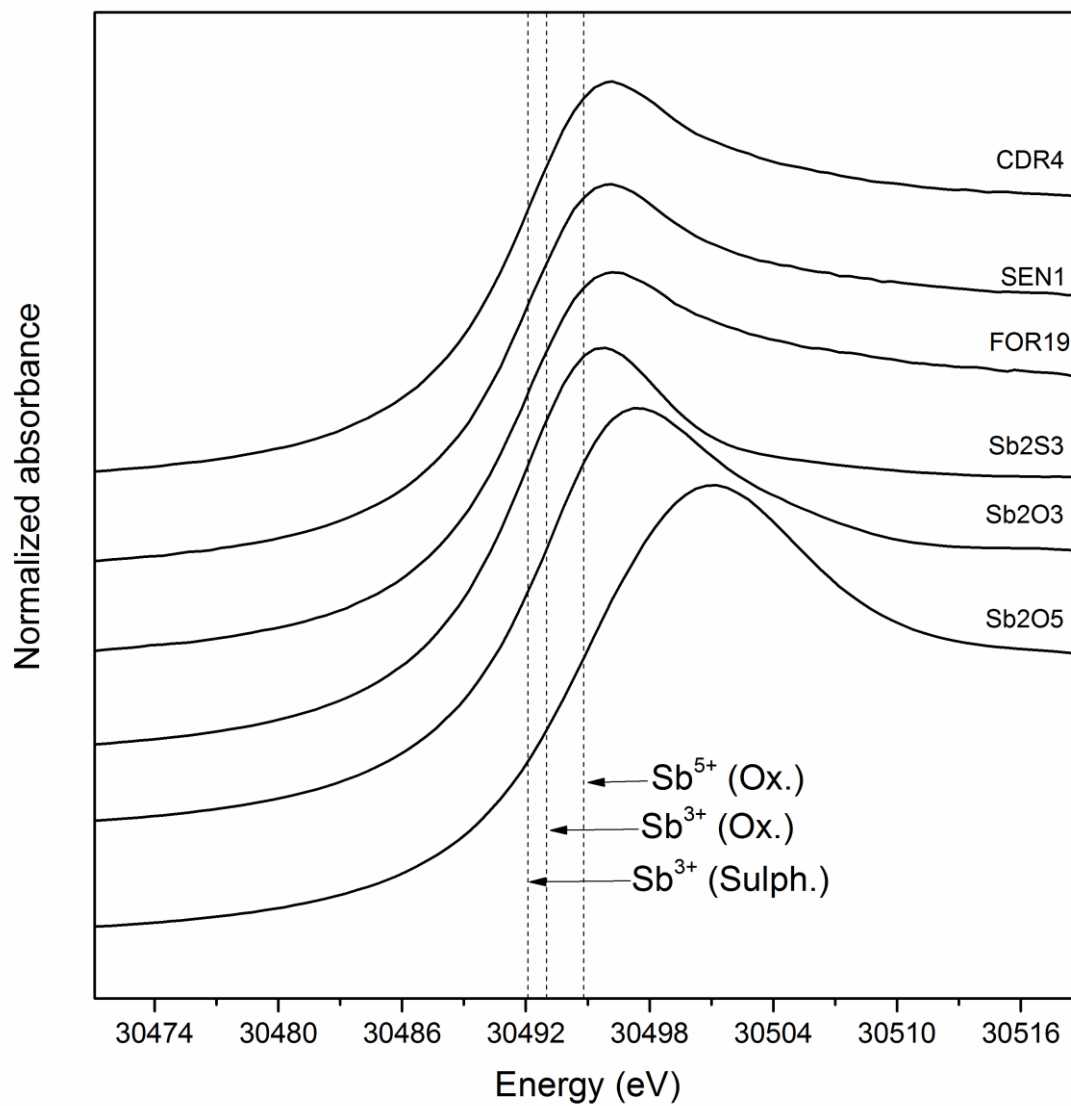
ACCEPTED



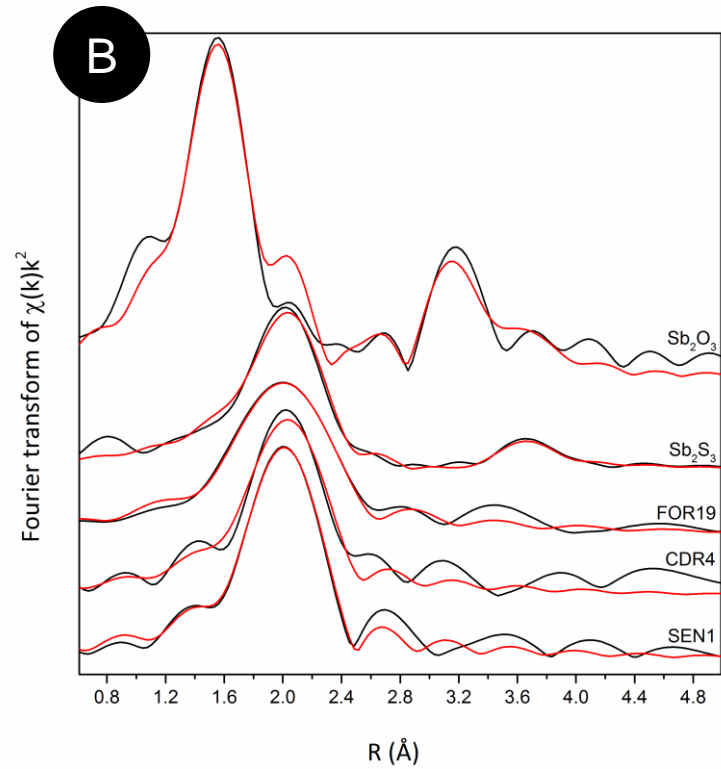
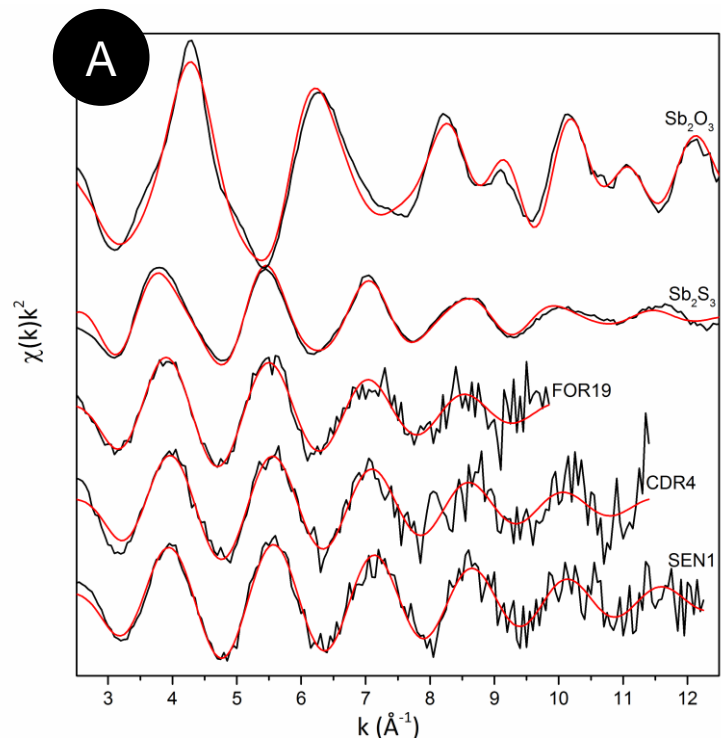


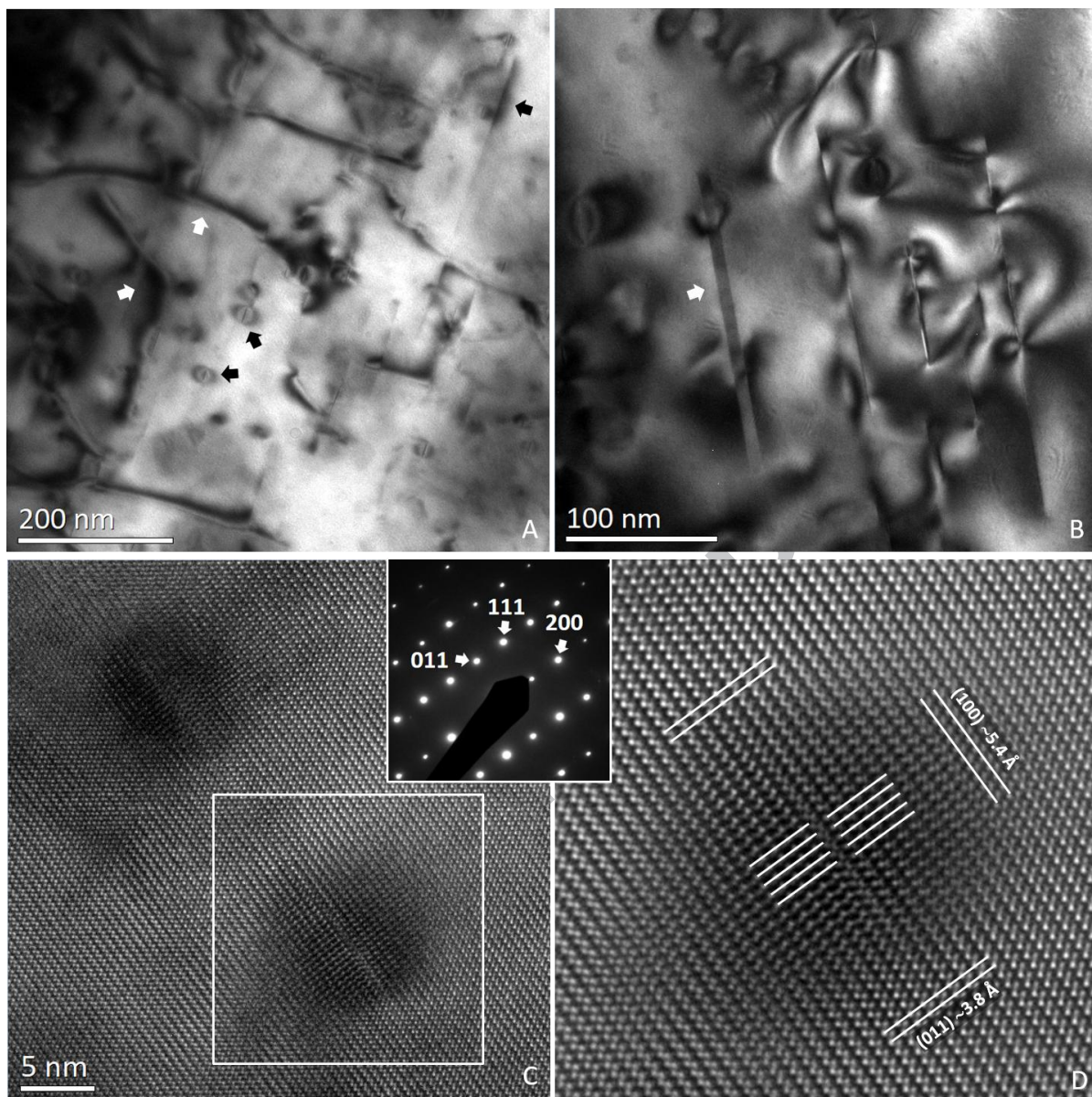


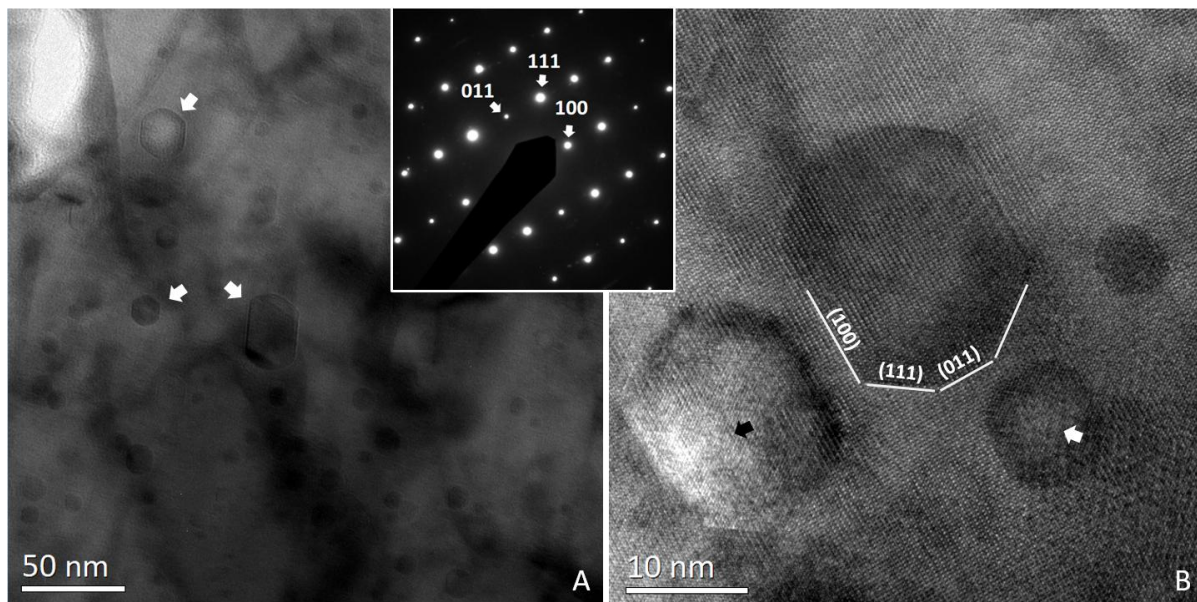
ACCEPTED



ACCE







ACCEPTED MANUSCRIPT

